Foraminiferal Mn/Ca as Bottom-Water Hypoxia Proxy: An Assessment of Nonionella stella in the Santa Barbara Basin, USA

I. Brinkmann, S. Ni, Magali Schweizer, V E Oldham, N B Quintana Krupinski, K. Medjoubi, A. Somogyi, M J Whitehouse, C M Hansel, Christine Barras, et al.

Paleoceanography and Paleoclimatology

AGU ADVANCING EARTH AND SPACE SCIENCE

RESEARCH ARTICLE
10.1029/2020PA004167

Key Points:

- Benthic foraminiferal Mn/Ca is explored as low-oxygen proxy using synchrotron-based X-ray fluorescence (XRF) nano-imaging and ion-beam trace-element analysis
- The new phylotype *Nonionella sp.* T6 is linked to *Nonionella stella* in a combined molecular-morphological species identification approach
- Foraminiferal Mn/Ca correlates positively with bottom-water dissolved oxygen within the narrow gradient of suboxia ($[O_2] < 10$ µmol/l)

Supporting Information:

Supporting Information may be found in the online version of this article.

Correspondence to:

I. Brinkmann,
inda.brinkmann@geol.lu.se

Citation:

Brinkmann, I., Ni, S., Schweizer, M., Oldham, V. E., Quintana Krupinski, N. B., Medjoubi, K., et al. (2021). Foraminiferal Mn/Ca as bottom-water hypoxia proxy: An assessment of *Nonionella stella* in the Santa Barbara Basin, USA. *Paleoceanography and Paleoclimatology*, *36*, e2020PA004167. https://doi.org/10.1029/2020PA004167

Received 20 NOV 2020
Accepted 4 OCT 2021

Foraminiferal Mn/Ca as Bottom-Water Hypoxia Proxy: An Assessment of *Nonionella stella* in the Santa Barbara Basin, USA

I. Brinkmann[1], S. Ni[1,2], M. Schweizer[3], V. E. Oldham[4,5], N. B. Quintana Krupinski[1,6], K. Medjoubi[7], A. Somogyi[7], M. J. Whitehouse[8], C. M. Hansel[4], C. Barras[3], J. M. Bernhard[4], and H. L. Filipsson[1]

[1]Department of Geology, Lund University, Lund, Sweden, [2]Centre for Environmental and Climate Research, Lund University, Lund, Sweden, [3]UMR 6112 LPG-BIAF, Université d'Angers, Université de Nantes, CNRS, Angers, France, [4]Woods Hole Oceanographic Institution, Woods Hole, MA, USA, [5]Now at University of Rhode Island, Kingston, RI, USA, [6]Now at Department of Earth and Environment, WSP Sweden, Malmö, Sweden, [7]Nanoscopium Synchrotron SOLEIL Saint-Aubin, Gif-sur-Yvette Cedex, France, [8]Department of Geosciences, Swedish Museum of Natural History, Stockholm, Sweden

Abstract Hypoxia is of increasing concern in marine areas, calling for a better understanding of mechanisms leading to decreasing dissolved oxygen concentrations ($[O_2]$). Much can be learned about the processes and implications of deoxygenation for marine ecosystems using proxy records from low-oxygen sites, provided proxies, such as the manganese (Mn) to calcium (Ca) ratio in benthic foraminiferal calcite, are available and well calibrated. Here we report a modern geochemical data set from three hypoxic sites within the Santa Barbara Basin (SBB), USA, where we study the response of Mn/Ca_{foram} in the benthic foraminifer *Nonionella stella* to variations in sedimentary redox conditions (Mn, Fe) and bottom-water dissolved $[O_2]$. We combine molecular species identification by small subunit rDNA sequencing with morphological characterization and assign the SBB *N. stella* used here to a new phylotype (T6). Synchrotron-based scanning X-ray fluorescence (XRF) imaging and Secondary Ion Mass Spectrometry (SIMS) show low Mn incorporation (partition coefficient $D_{Mn} < 0.05$) and limited proxy sensitivity of *N. stella*, at least within the range of dissolved $[O_2]$ (2.7–9.6 µmol/l) and $Mn_{pore\text{-}water}$ gradients (2.12–21.59 µmol/l). Notably, even though intra- and interspecimen Mn/Ca variability (33% and 58%, respectively) was only partially controlled by the environment, Mn/Ca_{foram} significantly correlated with both pore-water Mn and bottom-water $[O_2]$. However, the prevalent suboxic bottom-water conditions and limited dissolved $[O_2]$ range complicate the interpretation of trace-elemental trends. Additional work involving other oxygenation proxies and samples from a wider oxygen gradient should be pursued to further develop foraminiferal Mn/Ca as an indicator for hypoxic conditions.

1. Introduction

Marine environmental conditions are changing in oceans globally in response to recent climate change, and among these changes, decreasing seawater dissolved O_2 concentrations ($[O_2]$) have particularly severe implications for marine ecosystems (e.g., Halpern et al., 2008; Keeling & Garcia, 2002; Rhein et al., 2013). While these developments are recent and largely caused by current anthropogenic activity (e.g., Levin & Breitburg, 2015), comparable events have occurred in the past and can provide valuable analogs for modern-day and potential future changes. For this reason, the reduction of uncertainties in reconstructions of past environmental and oceanographic variations has become increasingly important in climate research (e.g., Koho et al., 2017; Lenz et al., 2015).

Progress has been made in the development of proxies for past oxygenation conditions—in particular the use of redox-sensitive trace elements (TE), such as benthic foraminiferal Mn/Ca (e.g., Barras et al., 2018; Glock et al., 2012; Groeneveld & Filipsson, 2013; Klinkhammer et al., 2009; Koho et al., 2015, 2017; McKay et al., 2015; Ní Fhlaithearta et al., 2010; Reichart et al., 2003), has gained much attention (see review by Tribovillard et al., 2006). Explorations of foraminiferal Mn/Ca under a range of hydrographic conditions, coastal low-oxygen regions (Groeneveld & Filipsson, 2013; Guo et al., 2019; Petersen et al., 2018), well oxygenated areas (Ní Fhlaithearta et al., 2018) and oxygen-minimum zones (Glock et al., 2012; Koho

et al., 2015, 2017; Reichart et al., 2003), indicate that the proxy's relationship to bottom-water oxygen (BWO) is most robust under hypoxic conditions ($[O_2] < 63$ μmol/l). However, difficulties persist in the interpretation of environment-proxy links, highlighting the need for a sound understanding of the regional geochemical regime, extensive calibrations, and validation of empirically established proxy relationships in modern marine sediments affected by hypoxia.

In situ microanalyses, such as ion probe with Secondary Ion Mass Spectrometry (SIMS), have been shown to be especially precise in proxy calibration studies of foraminifera (e.g., Balestra et al., 2020; Glock et al., 2012, 2019; Livsey et al., 2020; Remmelzwaal et al., 2019). By targeting selected spots of successive chambers individually, a temporal archive of TE concentrations from their calcareous tests and associated environmental variability can be generated in high resolution. The geochemical composition of foraminiferal tests is governed by both external environmental parameters (e.g., Epstein et al., 1951; Murray, 2014; Nürnberg et al., 1996; Pearson, 2012) and internal factors, such as microhabitat preferences, seasonality, ontogeny, ecology and biomineralization processes (e.g., Barras et al., 2018; Koho et al., 2017; van Dijk et al., 2019; Zeebe et al., 2008). While the empirical proxy relationship of foraminiferal Mn/Ca and ambient Mn availability is generally supported by both field and culture studies (e.g., Barras et al., 2018; Koho et al., 2017; Munsel et al., 2010), the pathways of Mn uptake and incorporation to the site of calcification during biomineralization, specifically remain a topic of active discussion (e.g., Barras et al., 2018; van Dijk et al., 2019, 2020). Difficulties in reaching a consensus between putative biomineralization models might partly be related to species-specific controls on calcification processes (e.g., de Nooijer et al., 2014), making an accurate identification of taxa essential for the reliable application of proxies. Morphological characters alone are not always sufficient to accurately identify foraminifera taxonomically (e.g., Deldicq et al., 2019; Pawlowski & Holzmann, 2014). However, taxonomic uncertainties can be avoided by combining morphological with genetic species characterizations (e.g., Bird et al., 2020; Darling et al., 2016; Hayward et al., 2004; Pawlowski & Holzmann, 2014; Roberts et al., 2016; Schweizer et al., 2005).

Here, we focus on *Nonionella stella* (Cushman & Moyer, 1930), a typical morphospecies of the Santa Barbara Basin (SBB) off southern California, USA, and neighboring basins of the California borderland. To confirm its taxonomic affinity, we present a molecular-morphological characterization based on DNA barcoding together with SEM imaging for detailed resolution of morphological features. *N. stella* is well established as indicator taxon for low-oxygen conditions (e.g., Bernhard et al., 1997). Nevertheless, it has been rarely used for geochemistry-based paleoceanographic reconstructions (Altenbach et al., 2012; Kawahata, 2019) and its TE composition has not previously been studied. Here we pair in a multi-technique approach SIMS *in situ* TE analyses, to determine the concentration of Mn, Mg and Sr, with state-of-the-art synchrotron radiation-based scanning XRF (X-ray fluorescence) multilength scale imaging, to map the Mn and Ca distribution in selected foraminiferal tests in high resolution.

The SBB, a hypoxic basin with a long history of paleoceanographic research, presents a promising setting to observe foraminiferal proxy responses to bottom- and pore-water redox processes. Investigating the impact of present-day hypoxia in the SBB will provide a modern analog for future paleoreconstructions of the Southern California margin and context for near-shore low-oxygen settings in general. This study documents TE information for *N. stella* for the first time, contributes to a more complete understanding of the proxy relationship of benthic foraminifera and redox environments on a larger scale, and also critically assesses the limitations in proxy applications.

2. Regional Setting

The SBB (Figure 1a; continental Southern California Borderland; USA; Eastern Pacific) is an underwater plane confined by tectonic sills, the Santa Barbara coastline, and Channel Islands (Figure 1). At depths below the sills (westward 475 m, eastward 230 m), the dissolved $[O_2]$ decreases rapidly (Bograd et al., 2002; Komada et al., 2016; Reimers et al., 1990), due to restricted bottom-water (BW) circulation, influence of the eastern North Pacific oxygen minimum zone (OMZ), and high primary productivity (e.g., Emmer & Thunell, 2000; Kienast et al., 2002; Reimers et al., 1996; van Geen et al., 2003). The seasonally variable influence of the California Current System on the SBB, predominantly equatorward circulation during spring, poleward from summer to winter (Harms & Winant, 1998; Lynn & Simpson, 1987), drives the water

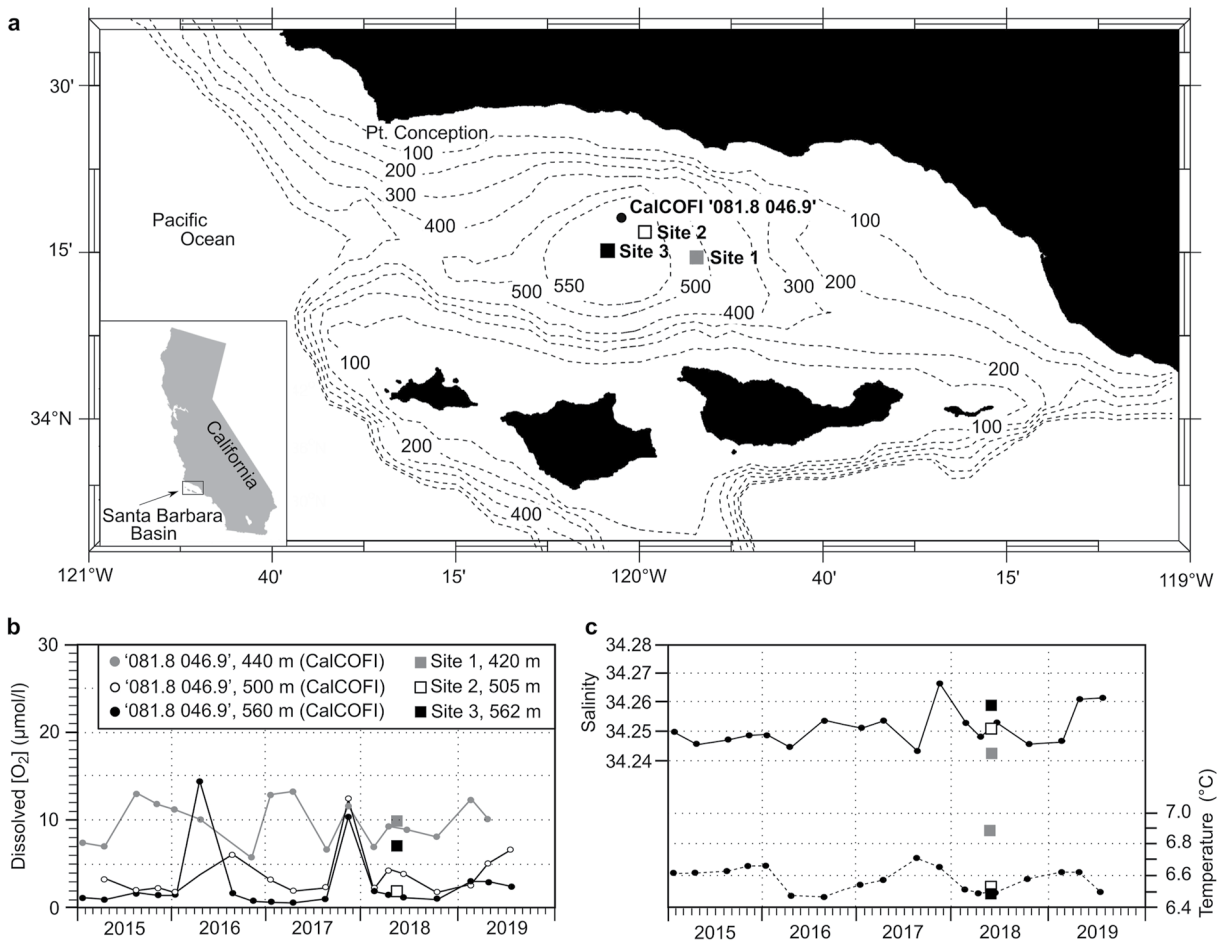

Figure 1. (a) Location of the Santa Barbara Basin (SBB) off the west coast of Southern California, USA, and bathymetric overview of the SBB. Map modified after Bograd et al. (2002). (b and c) Quarterly hydrographic measurements compiled from CalCOFI station '081.8 046.9' (CalCOFI, 2015–2019) and $CTDO_2$ data of this study (Bernhard, 2018): (b) dissolved $[O_2]$ from ~440, 500, and 560 m water depth and (c) salinity (straight line) and temperature (dashed line) of bottom waters (< 560 m). Positions of study sites indicated in (a) (site 1, 420 m, 34°18.6′N, 119°54.0′W; site 2, 505 m, 34°20.8′N, 119°59.0′W; site 3, 562 m, 34°19.2′N, 120°03.4′W).

exchange dynamics between the basin and open ocean. Renewal of deep- and bottom-waters through episodic upwelling introduces cold, more-oxygenated waters (Bray et al., 1999; Reimers et al., 1990). Nevertheless, deep basin waters (> 530 m) usually have $[O_2]$ < 3 µmol/l (e.g., Bernhard et al., 1997; Bernhard, Habura, Bowser, 2006). Over the past five decades, the California Cooperative Oceanic Fisheries Investigations (CalCOFI) Program has routinely collected quarterly hydrographic data (CalCOFI, 2015–2019) showing depletion and replenishment cycles of intermediate to bottom-water $[O_2]$ (Figure 1b for data of 2015–2019) and inter-annually relatively constant temperature (6°C) and salinity (34.25) (Figure 1c, Bograd et al., 2002; Komada et al., 2016).

3. Material and Methods

3.1. Study Sites and Sample Collection

The SBB was sampled in May 2018 (cruise SP1811, R/V *Robert Gordon Sproul*) at above sill-level site 1 (430 m; 34° 18.6'N, 119° 54.0'W) and deeper sites 2 (505 m; 34° 20.8'N, 119° 59.0'W) and 3 (567 m; 34° 19.2'N, 120° 03.4'W) (Figure 1a).

At each site, a 12-Niskin-bottle sampling rosette equipped with $CTDO_2$ was deployed to record water-column salinity (reported using the practical salinity scale), temperature, and dissolved $[O_2]$, and sample BW.

Duplicate cores were collected for core-tops (Ocean Instruments MC800 multicorer; 10-cm core tube inner diameter) and processed for respective analyses and sample collection immediately after retrieval. One core per site was transferred to a temperature-controlled van onboard the vessel (6°C) and dissolved [O_2] measured via micro-profiling at the sediment-water interface (SWI) and in pore waters (until [O_2] was undetectable; Unisense O_2 Microsensor OX-500, 200). Afterward, the top two cm of the profiled core were sliced in 0.5 cm sections as samples for foraminiferal analyses ('0–0.5 cm', '0.5–1.0 cm', '1.0–1.5 cm', and '1.5–2.0 cm'). At site 1, an additional ~3 mm thick layer of loose organic material, present above the SWI of the core, was sampled ("fluff"). Each 0.5-cm sediment slice was placed into an HDPE (High Density Polyethylene) bottle with roughly equal amounts of ambient BW. CellHunt Green (CHG) with CMFDA (5-Chloromethylfluorescein Diacetate) and dimethyl sulfoxide (DMSO) (all Saterah Biotech, Oregon, USA) was added to reach a final CHG concentration of 1 μM in the samples. The samples were incubated at 6°C for 10 h to allow living cells to take up the CHG epifluorescent tracer for later observation (Bernhard et al., 2004; Bernhard, Ostermann, Williams, & Blanks, 2006), and thereafter preserved by adding ethanol. The second core per site was sampled for pore-water TE analysis (dissolved Mn and Fe concentrations; [Mn] and [Fe]). To extract the pore water, cores were rapidly sectioned on deck (10 min processing time) in the sediment intervals 0.0–0.5 cm, 0.5–1.0 cm, 1–2 cm, 2–3 cm, and 3–4 cm, and then immediately centrifuged for 15 min. The supernatant from centrifuging (i.e., pore water) was filtered in a N_2-purged glove bag into new 3 mL conical tubes for each total dissolved Mn and Fe.

3.2. Geochemical Analysis of Pore-Water Samples

Total dissolved Mn in pore waters was measured using the porphyrin addition method (after Madison et al., 2011; modified by Oldham et al., 2017). First, the filtered sample was reduced with hydroxylamine hydrochloride (final concentration 20 μM), then the resulting Mn(II) was reacted with an added porphyrin reagent to form an Mn-porphyrin complex that absorbs at 468 nm, which was measured using a 1 cm cell coupled to a flame-mini UV-vis spectrophotometer (Ocean Optics) on the ship. The detection limit for this method is 50 nM, with an average reproducibility better than 2%. For dissolved Fe, pore-water samples were analyzed using the ferrozine method of Stookey (1970). This reaction forms a purple complex with a measurable absorbance at 562 nm, which was measured in a spectrophotometric microplate reader (Molecular Devices SpectraMax M3) on the ship. The detection limit for this method is 100 nM with an average reproducibility better than 4%.

3.3. DNA Barcoding and Taxonomic Identification of *Nonionella stella*

About 20 g of the surface-sediment from site 3 was sent refrigerated with BW by courier to the Laboratory of Planetology and Geosciences (LPG), University of Angers, France. There, the sediment was sieved over a 100-μm sieve and live specimens of *Nonionella* collected in seawater under a stereomicroscope. Four live specimens, distinguished by brownish dark green cytoplasm color and ability to gather fine sediment when left overnight (Schweizer et al., 2005), were selected, cleaned with a fine brush and air dried. Specimens were imaged with a Scanning Electron Microscope (SEM, EVOLS10, ZEISS, Germany) under low vacuum at the Service Commun d'Imageries et d'Analyses Microscopiques (SCIAM), University of Angers. Thereafter, specimens were individually placed in tubes with 60 μl deoxycholate (DOC) buffer (Pawlowski, 2000) to extract DNA. Foraminiferal DNA was amplified with a hot start (2 min at 95°C) PCR in a volume of 25 μl with 40 cycles of 30 s at 95°C, 30 s at 50°C, and 2 min at 72°C, followed by 10 min at 72°C for final extension with primers s14F3 and J2 for the first PCR and 30 cycles and an annealing temperature of 52°C (other parameters unchanged) for the nested PCR with primers s14F1 and N6 (Darling et al., 2016; Pawlowski, 2000). Positive amplifications were Sanger-sequenced directly at Eurofins Genomics (Cologne, Germany). DNA sequences were automatically aligned with available sequences of nonionids from GenBank with MUSCLE implemented in SeaView 4 (Gouy et al., 2010) and corrected manually to obtain an alignment of 512 sites. Among these sites, 316 did not show any polymorphism (61.7%). A maximum likelihood analysis was performed by PhyML implemented in Seaview under the GTR + G (General Time Reversible) evolutionary model with non-parametric bootstrapping (1,000 replicates). In addition, BioNJ (Neighbor Joining) analysis was run with Seaview under the Kimura's two parameter evolution model with non-parametric bootstrapping (1,000 replicates).

Table 1
Tabulation of Number of Specimens for Each Analysis Technique, Per Site, and Sediment Interval (cm)

	Site 1					Site 2				Site 3				Total number of analyzed specimens
	Fluff	0.0–0.5	0.5–1.0	1.0–1.5	1.5–2.0	0.0–0.5	0.5–1.0	1.0–1.5	1.5–2.0	0.0–0.5	0.5–1.0	1.0–1.5	1.5–2.0	
SIMS	9	8	10	11	11	10	11	10	10	10	7	9	11	127
μXRF				3										3
DNA										4 (0–1 cm)				4

3.4. Foraminiferal Sample Preparation for Geochemical Analyses

CHG-labeled *N. stella* specimens were picked from wet samples (> 100 μm) under an epifluorescence microscope (Nikon SMZ 1500 with Nikon Intensilight C-HGFI) and subsequently dried at room temperature. Three specimens (A–C) from site 1, 1.0–1.5 cm sediment depth, were selected for synchrotron radiation-based XRF imaging, and 127 specimens were selected for SIMS TE analysis (Table 1).

The specimens were treated with NaOCl (5%) for 2–5 h to remove cytoplasm (e.g., Lea et al., 1999; Mashiotta et al., 1999), rinsed three times with MilliQ water and stored in acetone overnight until epoxy-embedding. Prior to mounting, all tests were filled with epoxy involving several treatments with an acetone-epoxy-mixture in decreasing ratios. Epoxy-filled tests were embedded (EPO-TEK® 301) under vacuum in molds of 1 cm (synchrotron samples) or 2.5 cm diameter (SIMS samples) and dried at room temperature for 48 h. To expose central cross-sections of specimens, the epoxy mount surface was ground down (Struers LaboSystem with a LaboPol-60 and LaboForce-Mi specimen mover head, DiaDuo diamond emulsion 9 μm grain size) at the Department of Geology, Lund University, Sweden. Samples for synchrotron analysis were further abraded from the backside to a thickness of less than 1 mm to decrease scattering-effects of the epoxy on the XRF spectra, and the surface polished using a diamond emulsion of increasing fineness (6, 3, and 1 μm grain size; DiaDuo). SEM images were taken in low vacuum without coating (Tescan Mira3 High Resolution Schottky Field Emission SEM) at the Department of Geology in Lund to identify areas of interest. Samples for SIMS analysis were prepared with a mount thickness of 5 mm. The surface was polished at the NordSIMS laboratory, Natural History Museum, Stockholm, Sweden, using a Struers Rotopol-2 with Struers Pedemat (150 RPM, 5 N pressure) and polycrystalline diamond emulsion (9, 3, and 1 μm grain size; Akasel Aka-Spray Poly) combined with lubricant solution. Between polishing steps, mounts were cleaned with ethanol and quality of polishing assessed (Olympus BX60 microscope). The polished mounts were cleaned in an ethanol bath with sonication (Branson S800), coated with 5 nm of high-purity gold (BAL-TEC SCD 005 Sputter Coater) and SEM-imaged (Backscatter; TM4000Plus Hitachi). Prior to SIMS analysis the mounts were coated with an additional 20-nm high-purity gold layer to prevent surface charge development.

3.5. Synchrotron Scanning XRF Imaging

To investigate the spatial distribution of Ca and Mn across tests of *N. stella,* XRF imaging was performed at the NANOSCOPIUM hard X-ray nanoprobe beamline (150 nm beam size; Somogyi et al., 2015) hosted at the 2.75-GeV high-brilliance third-generation Synchrotron SOLEIL facility (Saint-Aubin, France). The samples were mounted vertically with an angle of 90° to the incident beam (11.2-keV X-ray energy) and the XRF spectra were collected by two SDD XRF detectors positioned at 20° to the reflecting sample surface. Elemental concentrations and distributions were mapped using the Flyscan continuous sample scanning technique (Medjoubi et al., 2013). Fast maps of entire specimens were acquired with 1 μm spatial resolution and 20 ms dwell time per pixel to guide the selection of regions of interest for higher resolution and longer dwell time zoom-in mapping (150 nm, 200 ms/pixel). The detection limit of [Mn] per pixel was in the ppm range for these high-resolution maps. The information depth was several tens of μm.

The PyMca software was used to fit the XRF sum-spectra to identify the elements present in the sample and possible spectral overlapping (Solé et al., 2007). The "zoom-in" maps of specimens A and C were acquired by three successive scans and rebound into single maps after dedicated image realignment. The elemental distribution maps were reconstructed by a homemade Matlab-code including dead-time correction,

showing intensities above the detection limit (95% confidence limit). Moreover, for each scan a sample mask was defined from the background corrected Ca intensity maps. All further image analyses described below used the Fiji distribution of ImageJ (Rueden et al., 2017; Schindelin et al., 2012). First, profiles perpendicular to selected test walls were drawn from XRF intensity maps to compare Mn and Ca intensity distributions (Figure S1) and tested for correlation (Pearson linear correlation) using the software package PAST 3.20 (Hammer et al., 2001). The Mn and Ca distribution maps were merged into color-coordinated composite images illustrating the co-localization of the elements. Second, the Mn to Ca ratio maps were created within the sample masks (see above). The relative intensity ratios could be converted to semi-quantitative concentration ratios (percentage mass and molar mass) by taking the measurement geometry, the XRF yields and detection efficiencies of the XRF spectral lines into account and assuming a calcite sample matrix (Jenkins, 1995). The ratios were reported as Mn/Ca_{XRF} to distinguish them from quantitative, SIMS-derived data.

3.6. SIMS Trace Element Analysis

Trace element concentrations of test walls were analyzed using a CAMECA ims1280 ion microprobe (NordSIMS Laboratory, Sweden). An in-house OKA calcite crystal served as reference material, as well as UWC-3 as secondary reference (provided by John W. Walley and Mike Spicuzza, Department of Geoscience, University of Wisconsin, USA) (Kozdon et al., 2009; Orland et al., 2014). The TE concentrations (^{55}Mn, ^{24}Mg, ^{88}Sr) in OKA were determined by laser-ablation ICP-MS analyses at the Department of Geology in Lund using a Bruker Aurora Elite (quadrupole) ICP-MS and a 193 nm Cetac Analyte G2 excimer laser installed with a two volume HelEx2 sample cell, giving Mn = 2327 ± 71 ppm, Mg = 662 ± 22 ppm, Sr = 11285 ± 303 ppm (mean values and standard deviations of 18 spots over three calcite grains for Mn and 24 spots on four grains for Mg and Sr). The analytical session (Table S1 for details) was setup to run automatically with standard-sample-standard bracketing. Each analysis was done with 300 shots at 10 Hz and a fluence of 3 J/cm^2 for the NIST glass and 2 J/cm^2 for the carbonate matrix materials (Table S1 for details). Baseline compositions were measured for 30 s before each measurement. U.S. National Institute of Standards and Technology SRM NIST610 was used as external calibration material (composition values as in GeoReM [Jochum et al., 2005] via http://georem.mpch-mainz.gwdg.de). Data reduction was done using Iolite software build within the Wavemetrics IgorPro using the X_Trace_Elements_IS data reduction scheme (Paton et al., 2011; Woodhead et al., 2007).

For each specimen, locations for three spots (if all areas of interest were exposed for analysis), one each on the final (n), penultimate (n-1), and antepenultimate (n-2) chamber walls, were preselected based on SEM images. The measurements were programmed manually to avoid stage reproducibility problems as the wall thickness is typically only double the instrument specification. Exact target areas within the thin walls were determined using scanning ion imaging of the ^{44}Ca signal with 1 nA $^{16}O_2^-$ from the Hyperion H201 RF plasma source rastered over a 10 × 10 μm area. The dynamic transfer optical system (DTOS), a synchronized raster in the secondary ion beam, generated the ion image in real time. This step also served to remove the gold coating and any potential surface contamination in preparation for analysis. Once the target area had been centered in the ion image, the primary beam was set to 300 pA, primary beam raster was reduced to 5 × 5 μm, the field aperture in the secondary beam was closed to limit the field of view on the sample to an effective 3 × 3 μm square and the DTOS was deactivated. Fine adjustments to positioning were then made using 1-μm steps in *x* and/or *y* to maximize the ^{43}Ca signal, as required. For standards, the surface was presputtered over a rastered 10 × 10 μm area for 90 s to remove the gold with the 1 nA beam, after which analytical settings were the same as for the target foraminifera. Prior to data acquisition, the secondary ion beam was automatically centered in the field aperture, the sample high voltage adjusted to maximize the signal transmitted through the 45 eV energy window and the mass calibration adjusted, all steps utilizing the ^{44}Ca signal. Each analysis then comprised 16 cycles through the species ^{24}Mg in the axial electron multiplier at mass resolution (M/ΔM) ~ 6000 (EM-ax; 2 s/cycle integration), ^{44}Ca in both EM-ax and an off-axis electron multiplier (M/ΔM) ~ 2500 (C; 0.5 s for both), ^{55}Mn in EM-ax (2 s), $^{40}Ca^{42}Ca$ in C (2 s), and $^{88}Sr+^{44}Ca_2$ in C (2 s). The ^{88}Sr signal was then corrected by subtracting the calculated $^{44}Ca_2$ from the combined $^{88}Sr + {}^{44}Ca_2$ signal. All element species were normalized to ^{44}Ca and concentrations determined relative to regularly interspersed measurements of the OKA reference material made under identical conditions using the concentration in OKA determined by laser-ablation ICP-MS analyses. The detection

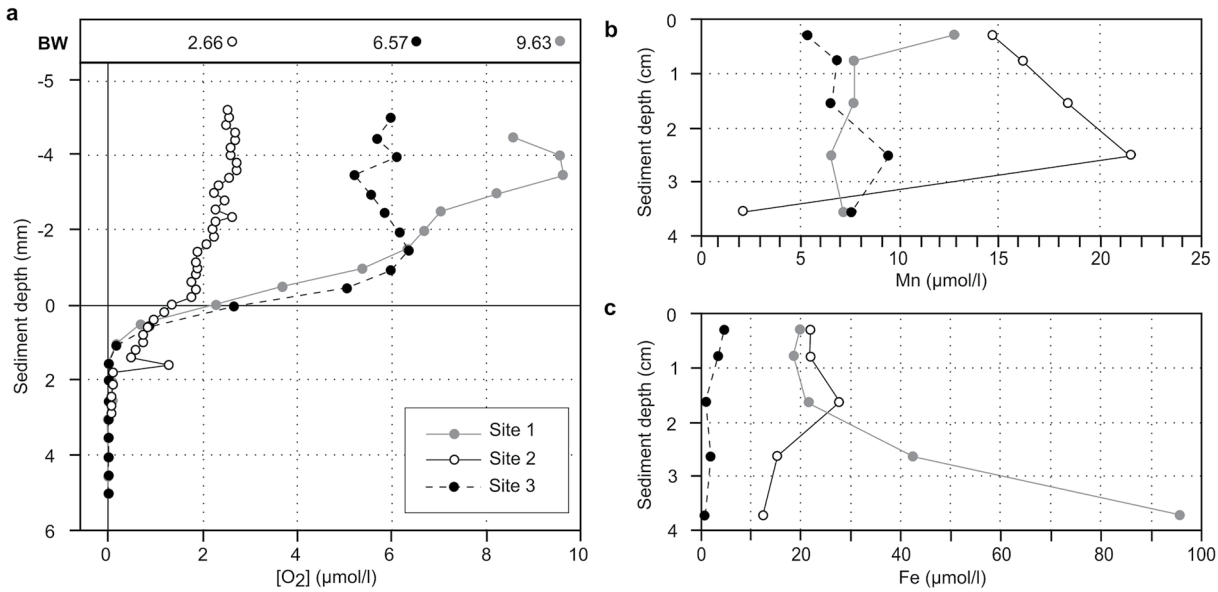

Figure 2. Profiles of physical and chemical conditions in sediment cores taken from the study sites. (a) Microprofiles of bottom- and pore-water dissolved [O_2] (200-µm steps for site 2; 500 µm for sites 1 and 3). Values of BWO acquired via CTD are indicated at graph top (Bernhard, 2018). (b and c) Pore-water TE concentrations across top 4 cm of sediment (b) Mn concentration, (c) Fe concentration. Note difference in unit for sediment depths of (a) and (b), and (c).

limit was below 0.2 ppm for Mn, 0.07 ppm for Mg, and 0.02 ppm for Sr and the reproducibility derived from the OKA standard ($n = 38$) was 2.7% for Mn, 7.0% for Mg, and 4.0% for Sr concentrations (average relative standard deviations, RSD), which translates directly to the reproducibility on TE ratios to Ca. The samples' TE ratios (Mn/Ca, Mg/Ca, Sr/Ca) were derived from the concentrations assuming a Ca concentration of 511700 µg/g (Chen & Simonetti, 2013).

To exclude potentially contaminated spots, the Mn/Ca data was paired with measurements of Mg/Ca and Sr/Ca and their correlations tested (Spearman's rank correlation coefficient). As the Mn/Ca data was non-normally distributed (Shapiro-Wilk's test), and in parts comprised variable specimen or sample numbers (heteroscedastic data), statistical analyses suitable for such datasets were used: Welch ANOVA or two-way PERMANOVA (Anderson, 2017; McDonald, 2014) for testing differences between chambers, sediment intervals and sites and Kruskal-Wallis and associated Mann-Whitney post-hoc tests for pairwise comparisons. Relationships between two variables were tested with the Pearson correlation coefficient (e.g., Mn/Ca_{foram} and BWO concentration). All statistical analyses were performed with PAST 3.20 (Hammer et al., 2001), and a p-value of < 0.05 was considered significant.

4. Results

4.1. Environmental Parameters

At all sites, both water-column temperature and [O_2] decreased from surface to bottom (by 6.5°C and 225–230 µmol/l, respectively; Figure S2; Bernhard, 2018), whereas salinity increased slightly (0.6; Figure S2; Bernhard, 2018). The halocline was at around 100 m water depth, after which temperature and salinity remained relatively uniform (BW = 6.52–6.87°C and 34.3–34.4). Dissolved [O_2] shifted several times throughout the water-column (site 1 at 100 and 250 m; site 2 at 195 m; site 3 at 75 m, 200 and 540 m). Most notable was a positive excursion in the deep-waters of site 3, increasing dissolved [O_2] from a minimum of 0.37–2.27 µmol/l (495–530 m) to a deep-water maximum of 8.89 µmol/l at 540 m depth (Figure S2). At the sampling date, BWO was 2.66 µmol/l at site 2, 6.57 µmol/l at site 3, and 9.63 µmol/l at site 1.

The oxygen concentration declined most steeply from the bottom- to pore-waters in sites 1 and 3 (Figure 2a), although [O_2] became non-detectable at approximately the same depth for all sites (~2 mm; Figure 2a).

At sites 1 and 3, the pore-water dissolved [Mn] were relatively consistent throughout the upper four cm of the sediment (6.6–12.7 and 5.08–9.4 μmol/l, respectively; Figure 2b). However, site 2 showed a dissolved Mn range of 2.12–21.59 μmol/l and included the highest measured dissolved Mn values of all sites, suggesting that this site contained an active Mn redox gradient (Figure 2b). To be able to compare the pore-water [Mn] (measured from 0.0–0.5 cm, 0.5–1.0 cm, 1–2 cm, 2–3 cm, and 3–4 cm) to foraminiferal TE concentrations (measured at 0.0–0.5 cm, 0.5–1.0 cm, 1.0–1.5, and 1.5–2.0 cm), we interpolated the pore-water [Mn] data to obtain additional approximate data points for the depth intervals 1.0–1.5 and 1.5–2.0 cm. Based on this interpolation we calculated 7.56 and 7.87 μmol/l Mn (site 1), 19.05 and 17.50 μmol/l (site 2), and 7.30 and 6.73 μmol/l (site 3) for the intervals 1.0–1.5 and 1.5–2.0 cm, respectively. Average $Mn_{pore\text{-}water}$ of the top 2 cm did not correlate with ambient BWO. At site 1, the pore-water dissolved [Fe] increased with depth and had the comparatively largest change in values (19.4–96.6 μmol) (Figure 2c). Conversely, dissolved [Fe] decreased down-core in sites 2 (after a subsurface peak at 1.5 cm depth) and 3. Site 3 had the lowest dissolved [Fe], by a factor of four to five.

4.2. Morphological Characterization and DNA Barcoding of *Nonionella stella*

The tests of the four specimens selected for molecular characterization were smooth with a trochospiral chamber arrangement and a rounded periphery. Larger tests were slightly elongated, as each newly added chamber was larger than the previous (Figure 3a). On the spiral side, the coiling was partially evolute (Figure 3a, SB064), whereas it was involute on the umbilical side (Figure 3a, SB063, SB065, SB066). The umbilicus was covered by a star-like extension of the chambers, with four to five points, and the last chamber extension covered the extensions of older chambers. The last whorl had seven to eight chambers. Sutures were curved backward and depressed with increasing depth from periphery to center. Pores were small and aggregated in groups (Figure 3b).

Two new DNA sequences were obtained (GenBank accession numbers MT591587–MT591588). Sequences were identical to each other and 99.8% similar to a sequence from GenBank identified as the morphospecies *N. stella* (AY818727; Bernhard, Habura, Bowser, 2006), also from SBB. The new sequences were aligned with a selection of other nonionid sequences retrieved from GenBank. Neighbor Joining and Maximum Likelihood gave the same phylogenetic tree topology (Figure 3c and S3). The nonionid sequences were grouped in six clades interpreted as different phylotypes (T1–T6). T1–T5 have been previously described in Deldicq et al. (2019), whereas T6 originated from the split of T4 into two clades and accordingly is here described as a new phylotype. The variation between phylotypes was mainly concentrated in three variable regions and 38.3% of the 512 sites showed polymorphism. The six phylotypes had a medium to very high statistical support (> 55/73) and relatively long branches. The trees were rooted on phylotype T5, as analyses with a wider data set (see Deldicq et al., 2019) placed this clade at the root of the nonionids studied here. The statistical support for grouping the phylotypes together was low (37/69 for the group T1 + T2 + T3) to medium (45/78 for the group T4 + T6), which was at least partially due to the low number of phylogenetically informative sites (196) available for analysis.

4.3. Distribution of Ca and Mn by Scanning XRF Imaging

Three specimens of *N. stella* were investigated for Ca and Mn distributions by synchrotron radiation-based scanning XRF nano-imaging (Figure 4). The Ca-fluorescence intensity maps distinctly showed the location of calcium-carbonate test material with a 1.5–2.0 μm wide zone of high intensity Ca signals, which is the $CaCO_3$ test wall. The Ca signal persisted, albeit weaker, in the inner test area, as the XRF signal was averaged through several tens of micrometers sample thickness, causing a projection image of the test parts within the epoxy. The Ca distribution was homogenous within test walls. On inner wall surfaces Ca appeared to be heterogeneously distributed in relatively regular patterns, potentially indicating the presence of pore spaces.

The Mn intensity was above detection limit only in some pixels of the fast 1 μm resolution overview images. In order to get a better insight into Mn distribution trends within whole specimens, the Mn and Ca images were binned (by 3 × 3 pixels) to create RGB distribution maps for choosing representative areas for high resolution mapping. The high-resolution images revealed that Mn generally followed the distribution of Ca

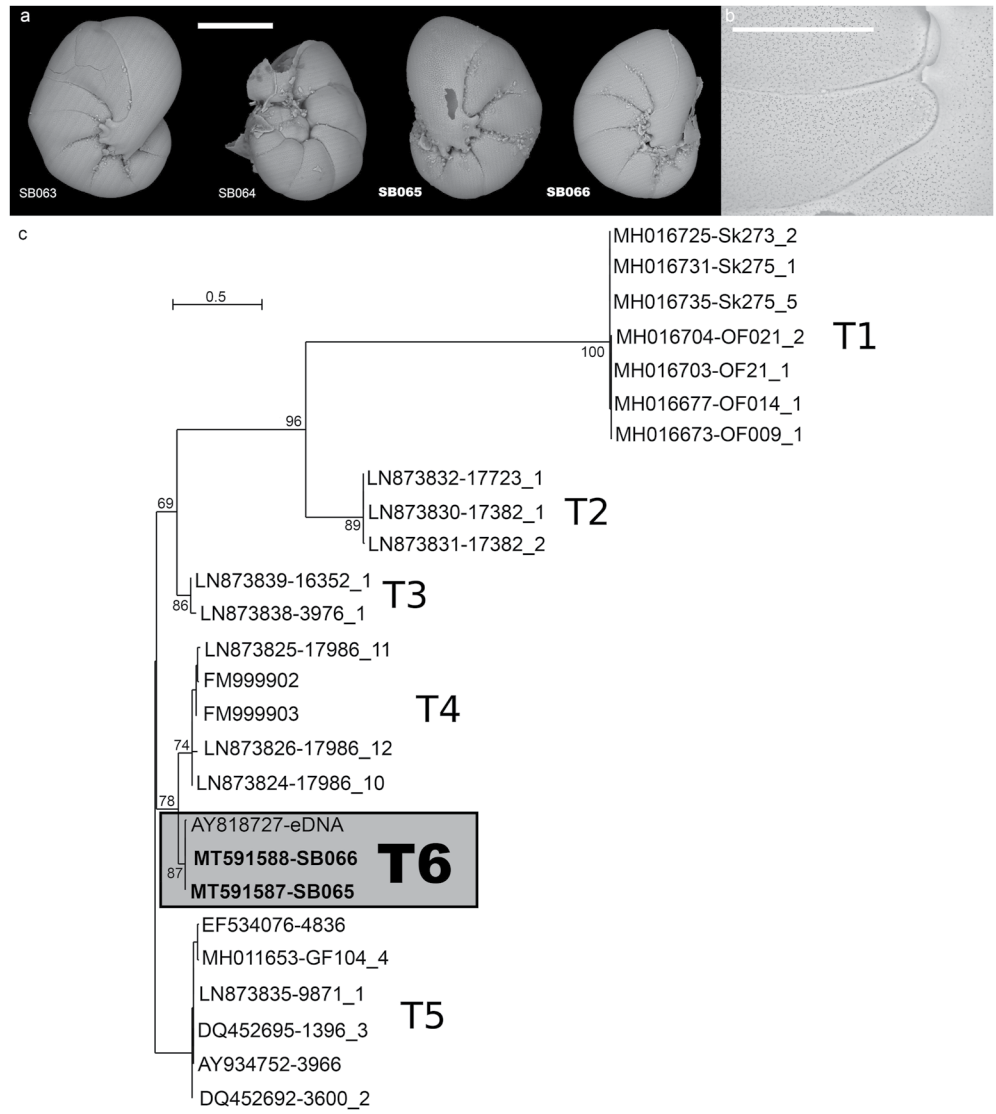

Figure 3. Morphological and genetic representation of *Nonionella stella*. (a) SEM images of *N. stella* from the Santa Barbara Basin. SB063, SB065, SB066: umbilical side, SB064: spiral side. Specimens in bold (SB065, SB066) gave DNA sequences. Scale bar 100 μm. (b) Close up of test surface with pores. Scale bar 50 μm. (c) Santa Barbara Basin *N. stella* in context of molecular phylogeny of sequenced nonionids based on partial SSU rDNA sequences inferred using ML method with the GTR + G model. The tree is rooted on the phylotype T5 and support values (BioNJ and ML) are indicated at the main nodes.

(Pearson linear correlation coefficient $\rho_{Mn/Ca}$ = 89–97) opposed to being present as a discrete phase. Within the calcite walls, Mn was heterogeneously distributed but showed no particular pattern at 150 nm scale. The semi-quantitative average Mn/Ca_{XRF} signals per investigated test area were 60 ± 17 μmol/mol (specimen A), 25 ± 25 μmol/mol (B), and 62 ± 17 μmol/mol (C). Mn/Ca_{XRF} varied by 28% and 27% (average RSD) in the selected areas of specimens A and C, respectively. Specimen B, having the lowest Mn content, showed a distinctly higher variation (100%), related to the high uncertainty of the Mn/Ca_{XRF} values with numerous pixels having low Mn content, close to the detection limit. Excluding pixels of Mn/Ca_{XRF} < 5 μmol/mol lowered its RSD to 60% (average Mn/Ca_{XRF} 38 ± 23 μmol/mol). Due to the semi-quantitative nature of the XRF-derived data, interpretations will be limited to the distribution and association of the analyzed TEs.

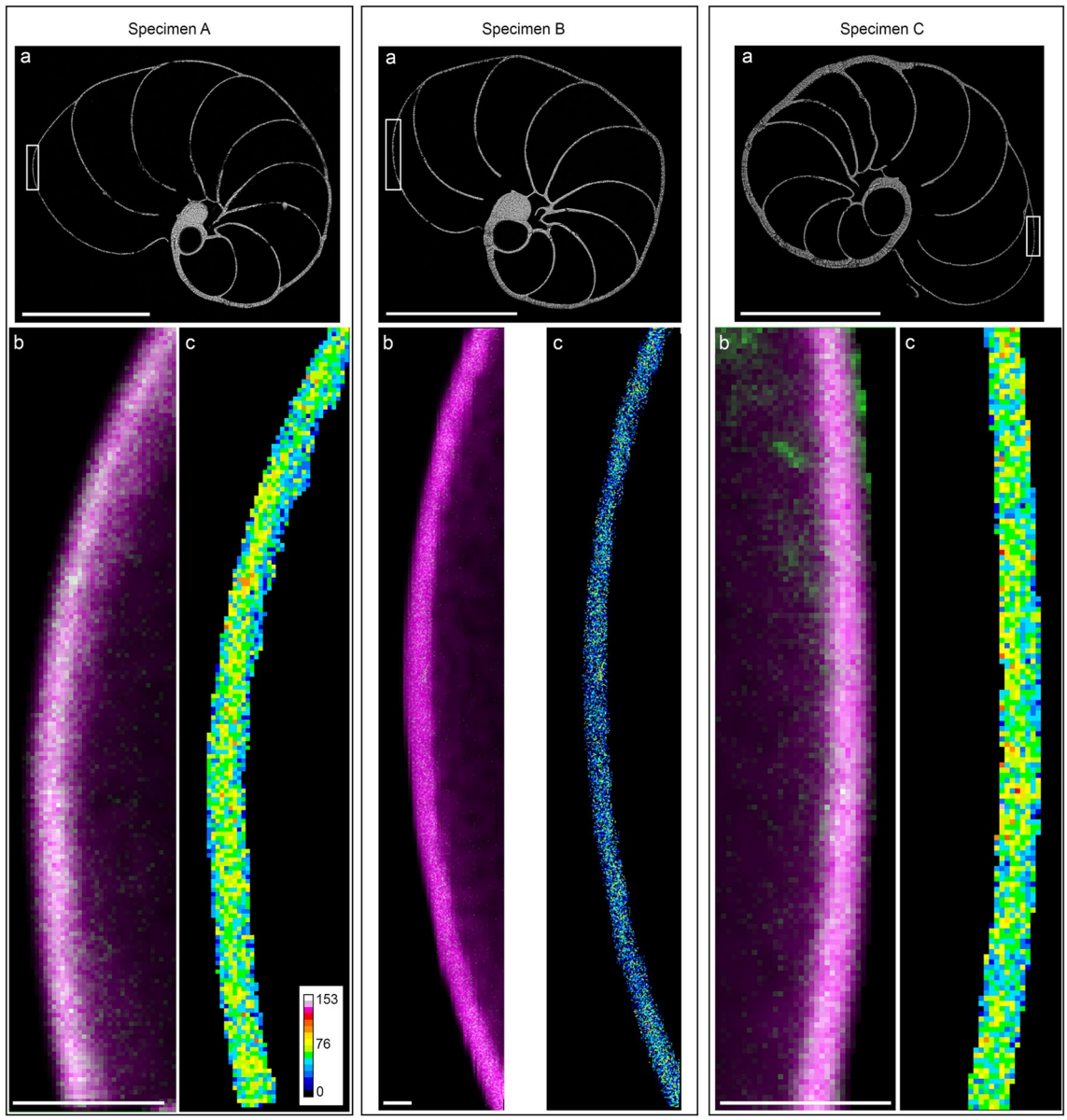

Figure 4. (a) Epoxy-embedded and polished specimens A, B, and C imaged with SEM. (b and c) "Zoom-in" X-ray fluorescence (XRF) elemental maps of selected regions of specimens A, B and C (position in respective tests indicated by white rectangle in a): (b) merged composite maps showing TE distribution of Ca (magenta) and Mn (green) (brighter colors indicate higher trace metal concentration; white to gray shades indicate colocation of Ca and Mn; black indicates concentrations below detection limit [95% confidence limit]); (c) semi-quantitative Mn/Ca maps (in μmol/mol) within sample masks based on Ca intensity (corresponding to test wall). Color scale bar corresponds to all specimens. Scale bars = 100 μm in (a), = 5 μm in (b and c). Note difference in length of imaged area of specimens A and C compared to B (i.e., white box in a and scale bars in b).

4.4. *In Situ* Elemental Concentrations Determined by SIMS

The *in situ* spot TE measurements performed on chamber walls of 127 *N. stella* specimens (Table 1) gave a total range of < 0.4–1596 μmol/mol for Mn/Ca, 0.6–43.5 mmol/mol Mg/Ca and 0.9–1.3 mmol/mol Sr/Ca. Mn/Ca signals were generally well below the empirically established ratio used in other studies to indicate the presence of (Mn-rich) diagenetic coatings (0.05 mmol/mol to ~0.15 mmol/mol; Boyle, 1983; Boyle & Keigwin, 1985; Delaney et al., 1985; Glock et al., 2012; Ohkouchi et al., 1994), as expected for live (CHG-labeled) specimens. Spots producing values distinctly outside this range (i.e., > 0.15 mmol/mol Mn/Ca) were excluded (three spots in total, 0.5–2.0 mmol/mol). In most chambers, TE ratios did not correlate (Spearman ranks r < -0.6 and > 0.6) or correlation was driven by a single spot, which accordingly was

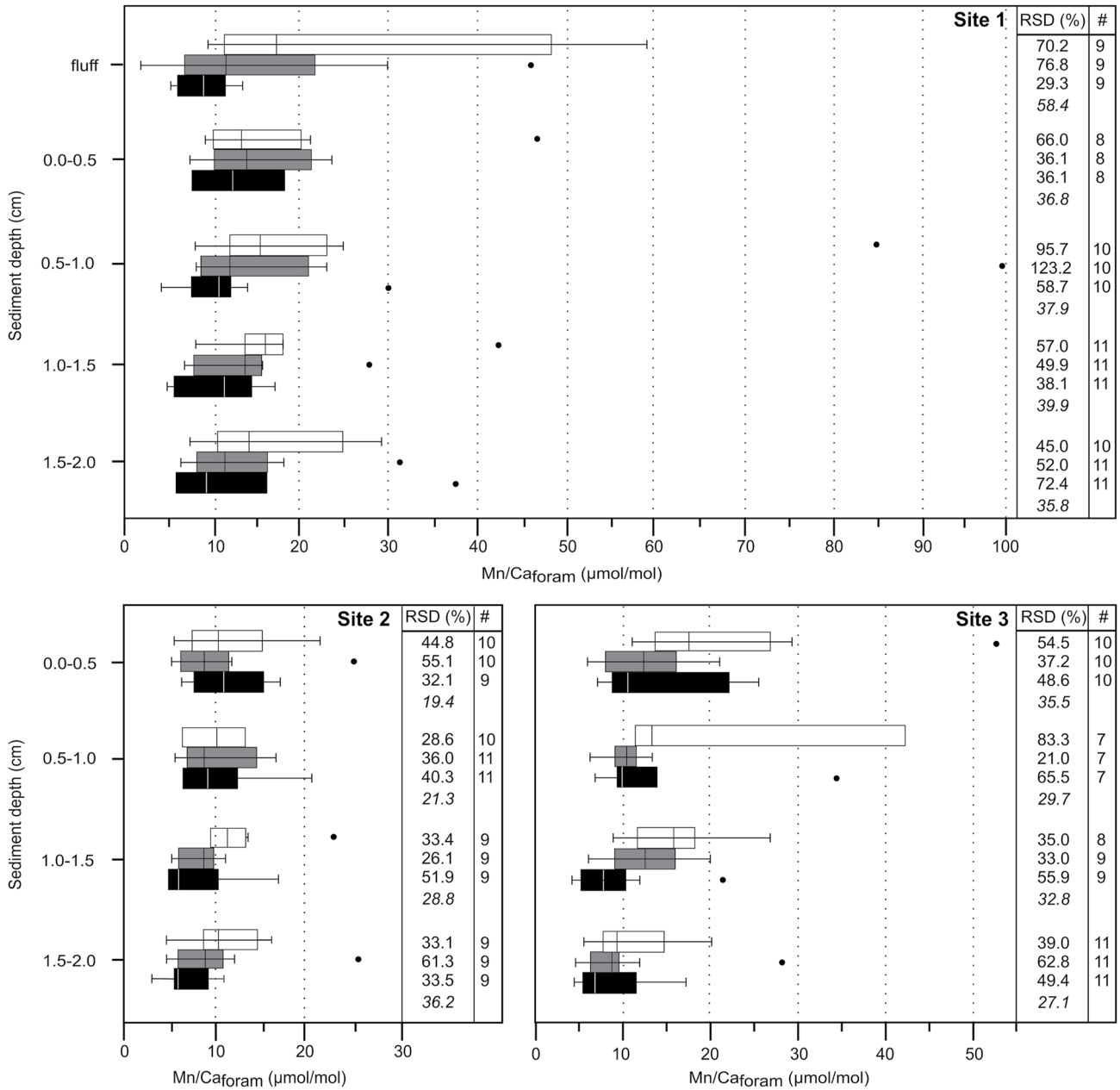

Figure 5. Box and whisker plots of the Secondary Ion Mass Spectrometry measurements of Mn/Ca (µmol/mol), average inter-specimen relative standard deviation (RSD %) per investigated site, sediment interval and chamber (n = white, n-1 = gray, n-2 = black) and number of analyzed specimens (#). The range of values per sample is visualized by boxes (interquartile range) and whiskers (extreme observations), with the vertical lines within boxes representing their median. Outliers are defined as values 1.5 times above the interquartile range and represented by dots. If no whiskers are visible the lowest and/or highest observations fall within the interquartile range.

excluded from further analyses (one analysis: n-2 chamber, 1.5–2.0 cm, site 2; Mg/Ca = 7.8 mmol/mol vs. average = 1.9 mmol/mol). Finally, Mn/Ca averages were 15.9 ± 13.4 µmol/mol (site 1; RSD = 41.4%), 10.2 ± 4.5 (site 2; RSD = 26.2%), and 12.0 ± 6.9 (site 3; RSD = 31.5%) (Figure 5, Table S2). Mg/Ca and Sr/Ca values are given in Table S3. SIMS, (quantitative) and scanning XRF-derived (semi-quantitative) Mn/Ca data differed on average by a factor of up to three to four. This was likely related to (a) the difference in Mn detection limits of the two methods, with the smallest [Mn] detected by SIMS having been below the XRF detection limit, and (b) methodological differences (e.g., measured spots per sample, different lateral spatial

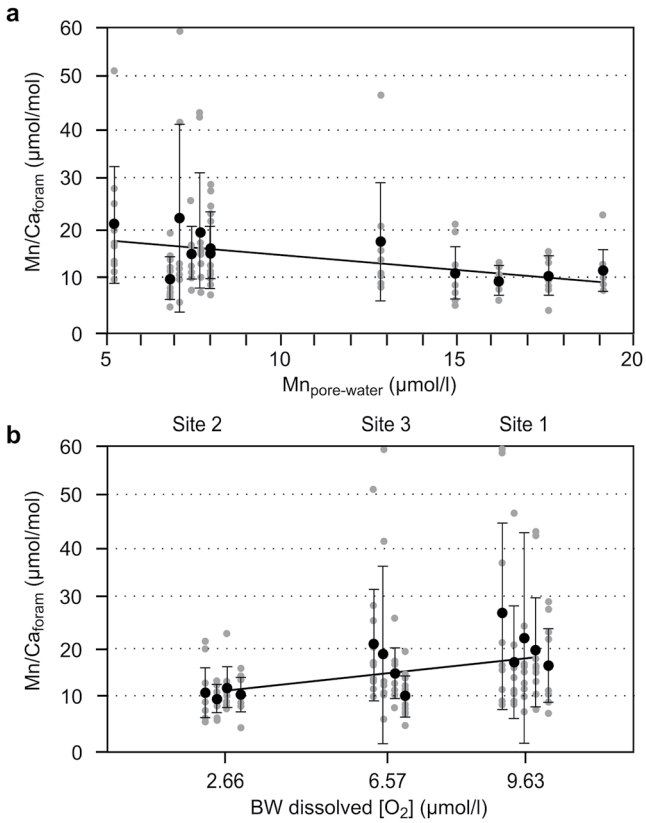

Figure 6. Individual Mn/Ca$_{foram}$ of n-chambers (gray) and their average with standard deviation per sediment interval (black) plotted against (a) pore-water [Mn] of respective sediment intervals (excl. "fluff") and (b) BW dissolved [O_2] per site (sediment intervals 0–2 cm from left to right, respectively; site 1 incl. "fluff"). Regression lines indicated for average Mn/Ca$_{foram}$ per sediment interval.

resolution, different signal penetration depth). The SIMS data forms the basis of the interpretations of Mn/Ca regarding proxy responses to pore-water [Mn] and BWO.

4.4.1. Inter- and Intrasite Variability

The Mn/Ca data showed variance ($p = 0.0004$; Welch ANOVA), with observably different RSDs for the investigated chambers, specimens, sediment intervals and sites (Figure 5). Mn/Ca from site 1 was different from site 2 (41.4 vs. 26.2% RSD; $p < 0.001$; Mann-Whitney pairwise). In site 1, variance of Mn/Ca was caused by differences between sediment intervals, specifically the difference between sample medians of the n-chamber from the "fluff" layer compared to underlying sediment intervals ($p < 0.001$; Mann-Whitney pairwise). Site 2, overall, showed no variance in Mn/Ca, but n-2-chambers differed ($p < 0.05$; Welch ANOVA) in 1.5–2.0 cm versus 0.0–0.5 cm and 0.5–1.0 cm sediment intervals. In site 3, both depth intervals and chambers caused variance ($p < 0.01$; Welch ANOVA).

4.4.2. Inter- and Intraspecimen Heterogeneity

Overall, the inter- and intra-specimen variability of Mn/Ca was relatively equal between all sites. Populations of one sediment interval generally showed higher variation (average $RSD_{inter} = 58\%$) than successive chambers of individuals (average $RSD_{intra} = 33\%$). Still, successive chambers differed ($p_{site1} = 0.008$, $p_{site2} = 0.001$, $p_{site3} = 0.030$; Kruskal-Wallis) (Figure 5), at least for selected sediment intervals and in most cases between n to n-1- and/or n-2-chambers (Mann-Whitney pairwise; $p < 0.05$). The "fluff" interval of site 1 showed distinctly higher intraspecimen variability compared to deeper sediment layers.

4.4.3. Correlation of Mn/Ca$_{foram}$ to [O_2] and [Mn]$_{pore-water}$

To test for correlations of Mn/Ca$_{foram}$ with environmental variables, only ratios of n-chambers were considered on the assumption of precipitation of most recent chambers (n) and environmental parameters measured during sampling being time-equivalent. Mn/Ca$_{foram}$ was uncorrelated with *in situ* pore-water [O_2]. Conversely, Mn/Ca$_{foram}$ (i.e., all specimens, one analysis per specimen on n-chamber; $r = -0.29$, $p = 0.002$) and averages of Mn/Ca$_{foram}$ per investigated sediment interval ($r = -0.67$, $p = 0.02$) correlated inversely with *in situ* pore-water Mn (Figure 6a). Both individual Mn/Ca$_{foram}$ values ($r = 0.31$, $p = 0.001$) and their average values per sediment interval ($r = 0.63$, $p = 0.02$) correlated positively with ambient BWO concentrations of each site, although the standard deviations are very high (Figure 6b).

5. Discussion

5.1. Influence of BWO Conditions on Mn and Fe Pore-Water Geochemistry

The water-column [O_2] profiles document the transport of oxygen-depleted waters into the basin and suboxic ([O_2] < 10 µmol/l) BW for all investigated sites (Figure S2). Site 3 appears to have recently received an input of slightly more-oxygenated waters, leaving its BWO, while still within the suboxic range, markedly higher than usual for site 3 (0.1–3 µmol/l vs. 6.6 µmol/l; e.g., Bernhard et al., 2003, 2010; Reimers et al., 1990, 1996).

Pore-water [Mn] measured in May 2018 are within the typical range for SBB surface sediments (10 µmol/l [Mn] at < 18 µmol/l [O_2]; Ivanochko & Pedersen, 2004; Reimers et al., 1996) and also OMZs (< 10–20 µM [Mn] at < 22 µmol/l [O_2]; e.g., Koho et al., 2017; Law et al., 2009; van der Weijden et al., 1999). Usually, under hypoxic BW conditions, microbial reduction of redox-sensitive elements causes steep redox gradients below the SWI (e.g., Aller et al., 1990; Burdige, 1993; Thamdrup, 2000), and dissolved [Mn] can reach up

to 500 μmol/l in surface sediments of coastal marine settings (e.g., Goldberg et al., 2012; Sulu-Gambari et al., 2017). This leads to an inverse correlation of pore-water dissolved Mn in surface sediments with BWO, as Mn is increasingly reduced during anaerobic bacterial respiration as oxygen depletes in surface sediments (e.g., Aller et al., 1990; Burdige, 1993; Thamdrup, 2000). This same inverse correlation is also assumed between foraminiferal Mn/Ca and BWO (e.g., Koho et al., 2015); hence its proxy potential. In the SBB, the situation is different, with BW dissolved [O_2] routinely below 10 μmol/l (see Figure 1b) and shallow oxygen penetration into the sediment (< 2 mm; Figure 2a). Under these conditions, mechanisms leading to depletion rather than accumulation of dissolved Mn dominate in surface sediments (e.g., Law et al., 2009; Sulu-Gambari et al., 2017; van der Weijden et al., 1999), resulting in very low concentrations of dissolved $Mn_{pore\text{-}water}$ (< 25 μmol; Figure 2b).

The dissolved [Fe] at site 1 (Figure 2c) matches typical values of the SBB's surface sediment pore-waters at comparable BWO conditions (60–120 μmol/l [Fe] at BWO < 15 μmol/l; Kuwabara et al., 1999; Zheng et al., 2000). With decreasing BWO, dissolved Fe becomes less abundant in surface sediments, as exemplified by site 2 and 3 (Figure 2c) and previous studies ([Fe] 40–60 μmol/l at BWO < 5 μmol/l [Reimers et al., 1996; Zheng et al., 2000]). As re-equilibration of sediment redox states to changes in [O_2] requires time (e.g., Burdige & Gieskes, 1983; Reimers et al., 1996), low dissolved [Fe] of site 3 (< 5 μmol/l) may represent an imprint of recent BWO concentrations of < 5 μmol/l, as suggested above.

5.2. Mn/Ca_{foram} as Proxy of Environmental Conditions

5.2.1. Response of Mn/Ca_{foram} to Pore-Water Mn Availability

The XRF maps of *N. stella* cross-sections show Mn hosted in the calcite lattice, as indicated by the colocation of Mn and Ca signals within the test wall (Figure 4b), although rare, localized spots of discrete Mn do appear (Figure 4c, specimen C). Mn occurring within the foraminiferal calcium-carbonate tests is a prerequisite for the proxy application, indicating direct incorporation of Mn as opposed to precipitation as discrete phases such as Mn (oxyhydr)oxide or carbonate coatings. It further suggests that the SIMS-derived Mn/Ca_{foram} values reliably represent the composition of the test wall.

Mn uptake into tests is generally assumed to positively relate to Mn bioavailability in the sedimentary (micro-) environment, which in turn is largely controlled by BWO (e.g., Guo et al., 2019; Jorissen et al., 1998, 2007; Mackensen et al., 2000; McCorkle et al., 1990; Ní Fhlaithearta et al., 2018; Tachikawa & Elderfield, 2002). This positive correlation has been validated for benthic foraminifera in controlled laboratory experiments with varying ambient dissolved [Mn] (Barras et al., 2018). Contrary to these results, our data show a slightly inverse correlation between Mn/Ca_{foram} and $Mn_{pore\text{-}water}$ (Figure 6a). Although statistically significant, the high standard deviation in the foraminiferal Mn/Ca per sediment interval and the narrow range of $Mn_{pore\text{-}water}$ encountered in our study area could explain the absence of the expected positive correlation. These uncertainties limit interpretations of the observed relationship in this study's data.

Another potential explanation could be a contribution of Mn(II) and Mn(III) in varying degrees to the total dissolved [Mn], as obtained in this study. While both soluble Mn(II) and Mn(III) are potentially bioavailable (e.g., Madison et al., 2011; Oldham et al., 2015; Trouwborst et al., 2006), foraminifera would incorporate only Mn(II) (van Dijk et al., 2019). A recent culturing study on large benthic foraminifera hypothesized sea-water carbonate chemistry as a potential factor in Mn speciation and foraminiferal incorporation (van Dijk et al., 2020). However, the significance of this effect versus differences in pore-water [Mn] driving foraminiferal Mn/Ca remains to be determined. Considering the extreme oxygenation and redox environment of SBB, we assume changes in the carbonate system, if present, to be a negligible factor to explain the observed Mn/Ca trends.

The observed inverse relation between Mn/Ca_{foram} and $Mn_{pore\text{-}water}$ may also hint at a spatial and/or temporal offset between measured pore-water Mn and ambient conditions during test biomineralization (see e.g., for [Fe] in Glock et al., 2012). This concerns both pore-water dissolved element concentrations being highly dynamic on small spatial and temporal scales, as well as biological factors causing uncertainties in the effective Mn pore-water concentrations during chamber precipitation. Small-scale migration of specimens within the sediment can blur distinct trends between pore-water and foraminiferal signals, particularly in dynamic redox environments (e.g., Ní Fhlaithearta et al., 2018; Petersen et al., 2018). Further, chamber

formation, which typically occurs within a few hours (Keul et al., 2013; de Nooijer et al., 2009, 2014), cannot unambiguously be assigned to a specific point in time. Although *N. stella* tests grow rapidly over a relatively restricted period (a few months; Bernhard & Reimers, 1991; Corliss & Silva, 1993), benthic foraminifera in general live for several months after reaching maturity, with life spans of up to two years (Murray, 2014), and biomineralization processes may be halted under unfavorable conditions. By extension, these effects can also influence the establishment of a proxy relationship between Mn/Ca_{foram} and BWO and cause intra- and inter-specimen variability within samples.

5.2.2. Response of Mn/Ca_{foram} to Bottom-Water Oxygenation

In SBB, Mn/Ca_{foram} show a positive trend with BWO (Figure 6b), comparable to previous observations of Mn/Ca in tests of *Bolivina spissa* from the OMZ off Peru (2–37 μmol/l $[O_2]$; Glock et al., 2012). In SBB, as in OMZ areas, suboxic conditions prevail and seasonal variations are within a small range of $[O_2]$. In this case, dissolved [Mn] in surface sediments are low despite reducing conditions, as particulate Mn fluxes to the sediment are low (see discussion Section 5.1). Only with slightly rising oxygen conditions Mn becomes available again for re-mobilization, as it is oxidized and precipitates at the sediment surface. Thus, within this limited oxygen gradient at the low end of hypoxia, the relation between Mn/Ca_{foram} and BWO seems to be positive (see also Glock et al., 2012), opposite to the trend expected in hypoxic conditions (i.e., inverse correlation).

While all sites remained within the suboxic range in the months preceding sampling (Figure 1b), given the narrow $[O_2]$ gradient even small deviations between measured and effective BWO require consideration (compare Section 5.2.1). Discrepancies are conceivable for site 3 if n-chamber precipitation occurred prior to the recent introduction of more-oxygenated waters (see Results Section 4.1 and Discussion Section 5.1). However, the inferred positive trend in the proxy relationship under suboxic conditions remains supported even assuming lower BWO for site 3, when considering the Mn/Ca_{foram} variability ($r = 0.18–0.25$, $p = 0.006–0.04$, testing individual Mn/Ca_{foram} and BWO of 0.1, 1, 2, 3 μmol/l $[O_2]$, respectively; not significant for average Mn/Ca_{foram}).

Our results highlight the fact that in the development and calibration of Mn/Ca as proxy of BWO concentrations the overall oxygenation regime of the study area (i.e., sub- vs. hypoxia) should be considered, and that the proxy sensitivity might be limited under suboxic conditions and/or over narrow oxygenation gradients. Using other redox proxies in tandem could aid in paleoenvironmental applications.

5.2.3. Potential Effects of Environmental Variability on Mn/Ca_{foram}

The previous sections suggest that averaging Mn/Ca over several specimens within one sample (i.e., theoretically time-equivalent), and over depth intervals, makes trends in relation to BWO more evident by evening out Mn/Ca variability. Still, this variability in itself can be highly informative about seasonal or local environmental driving factors (e.g., Petersen et al., 2019).

A substantial difference in Mn/Ca_{foram} variability is evident between the sites (41.4 vs. 26.2% RSD in site 1 and 2, respectively), presumably driven by their different oxygenation regime. Lower BWO, as prevalent in sites 2 and 3 (Figure 1b), potentially produces a more stable sedimentary Mn geochemistry even over longer time spans ($RSD_{intra} < 36\%$ vs. $> 36\%$ at site 1), as redox processes may dominantly take place in the water column (e.g., Law et al., 2009). The recent injection of more-oxygenated waters could explain the slightly elevated inter-specimen variability in site 3 (32% RSD_{site}). It thereby forms a gradient to the highest variability observed in the shallower site 1 (41% RSD_{site}), which is characterized by more frequent BWO variability (Figure 1b). Further, Glock et al. (2012) proposed that under higher BWO, foraminifera may more readily migrate vertically in the sediment, exposing them to a wider range of pore-water [Mn].

Even higher variability is observable in the "fluff" layer of site 1 (Figure 5), indicating highly dynamic redox cycling. We attribute this to higher organic matter content, porosity, and associated oxygen permeability, and/or denitrification activity (incl. potentially by *N. stella* itself; Bernhard et al., 2012; de Villiers, 2005 and references therein) within the 'fluff'. The coupling of Mn oxidation with denitrification (e.g., Luther et al., 1997; Vandenabeele et al., 1995) and rapid metabolic reactions to fluxes in N and Mn may cause higher micro-scale variability in Mn bioavailability, which is registered by Mn/Ca_{foram}. This effect seems to only concern n- and n-1 chambers, potentially indicating a distinct shift in environmental conditions after the

biomineralization of n-2 chambers. This could be linked to the formation of the "fluff" itself and active or passive migration of the foraminifera into this surficial layer.

Next to environmental changes, it is well documented for benthic (and planktonic) foraminifera that intrinsic factors can cause variation in TE signals (e.g., Davis et al., 2020; Petersen et al., 2018; Sadekov et al., 2008). Such factors are generally attributed to vital or ontogenetic effects, as well as genetic differences within species that influence physiological mechanisms of biomineralization (e.g., Barras et al., 2018; Diz et al., 2012; Elderfield et al., 1996, 2002; Erez, 2003; Filipsson et al., 2010; Hintz et al., 2006; Raitzsch et al., 2010). To identify intrinsically driven variability, precise taxonomic identifications, and the consideration of species-specific impacts on biomineralization are vital.

5.3. Mn Incorporation in *N. stella*

5.3.1. Taxonomic Assignment

Several *Nonionella* morphospecies, bearing a star-like extension of the chambers covering the umbilicus, are described, such as *Nonionella digitata* Nørvang (1945), *Nonionella opima* Cushman (1947) or *Nonionella stella* Cushman and Moyer (1930). *Nonionella digitata* is restricted to the Arctic region (Hayward et al., 2020), whereas *N. opima* is identified in the Gulf of Mexico, the Mediterranean and the Bay of Biscay (Hayward et al., 2020) and *N. stella* is considered a cosmopolitan species (Asteman & Schönfeld, 2016). However, a recent molecular study shows specimens identified as *N. stella* in the Skagerrak, NE Atlantic, forming a separate clade from *N. stella* identified off California (Deldicq et al., 2019), and should be named differently. Therefore, the star-like extension is not a sufficient morphological criterion to define the species and the distribution of the morphospecies *N. stella* needs to be reconsidered.

Among the other clades presented in Deldicq et al. (2019), the phylotype T4 harbors a specimen from the SBB morphologically identified as *N. stella* (Bernhard, Habura, et al., 2006) and other genetically closely related specimens sampled in Namibia (accession numbers FM999902–3) and the Adriatic Sea (Holzmann & Pawlowski, 2017), unfortunately with no published image of the test. As previously suspected (Deldicq et al., 2019), T4 is now split into two phylotypes, T4 with the unidentified nonionids from Namibia and the Adriatic Sea, and T6, newly defined in this article, for the SBB individuals.

The morphospecies *N. stella* is defined after specimens collected in the San Pedro Basin, off California (Cushman & Moyer, 1930). As the SBB individuals (*Nonionella* sp. T6) share similar morphological criteria (star-like umbilical extension, depressed sutures and elongated shape) and were collected only 200 km away from the holotype locality, their assignment as *N. stella* seems logical. Nevertheless, sequencing of topotypic material would be desirable to confirm this taxonomic identification (following Bird et al., 2020; Darling et al., 2016; Roberts et al., 2016).

5.3.2. Intrinsic Mn/Ca Variability in *N. stella*

Overall, the intra-specimen Mn/Ca variability of *N. stella* is comparable to previously reported values for field-collected benthic foraminifera (30%–50%; Glock et al., 2012; Koho et al., 2017; McKay et al., 2015; Ní Fhlaithearta et al., 2018; Petersen et al., 2018). Estimates of the contribution of intrinsic and extrinsic factors are only possible with laboratory calibration studies characterized by constant physico-chemical parameters. Barras et al. (2018) document intrinsic variability for *Ammonia tepida* (25%–85%) and *Bulimina marginata* (12%–14%) under geochemical conditions comparable to those encountered in the SBB ($[Mn]_{seawater}$ = 2.4 and 11.5 μmol/l). For *A. tepida,* ontogenetic effects contribute up to 57% to the variability, particularly at low ambient [Mn] (Barras et al., 2018). Additionally it has been shown that European representatives of the morphospecies *A. tepida* belong to several genetically distinct species (Hayward et al., 2004; Richirt et al., 2019), potentially explaining the large variability encountered in this taxon. *Nonionella stella* shows overall no significant chamber-specific difference in Mn/Ca, suggesting ontogeny-independent Mn uptake at least in the most recent chambers. The range of specimen-specific variability for previously investigated species also corresponds relatively well to the Mn/Ca heterogeneity observed in the XRF ratio maps (27%–28%, specimens A and C; Figure 4c).

Intrinsic factors may superimpose on environmentally controlled signals, and their contribution to the total variability must be considered in the interpretation of observed Mn/Ca trends with regards to BWO history.

Still, intrinsic variability does not limit the application of foraminiferal Mn/Ca as paleo-proxy, if calibrated successfully and on the species-level.

5.3.3. Species-Specific Control on Mn Partitioning by *N. stella*

As this is the first report of the TE composition of *N. stella* (average Mn/Ca = 13.81–26.56 μmol/mol; Figure 5, Table S2), related taxa *N. turgida* and *Nonionellina labradorica* (see Figure 3c, T3 linked to *N. turgida* and T5 to *N. labradorica*) are consulted as points of reference to compare the general Mn content of this group. Specimens collected from the western Baltic Sea (BWO = 104–193 μmol/l; $Mn_{bottom\text{-}water}$ = 0.1–0.2 μmol/l; Groeneveld et al., 2018) have distinctly higher Mn/Ca ratios by a factor of 100 (1.3–2.9 mmol/mol for *N. labradorica* and 1.1 mmol/mol for *N. turgida*). However, the pore-water [Mn] was not measured by Groeneveld et al. (2018) and might be higher than in SBB. Indeed this area of the Baltic Sea is only subject to seasonally hypoxic conditions (BWO > 40 μmol/l; see Groeneveld et al., 2018 and references therein), which may facilitate steeper redox gradients in surficial sediments, and associated higher dissolved Mn availability, opposed to the severely oxygen-depleted SBB environment (see discussion Section 5.1). On the other hand, *N. labradorica* from the NE Japan margin (BWO = 33–112 μmol/l; $Mn_{pore\text{-}water}$ < 5 μmol/l; Koho et al., 2017) produces calcite with lower Mn/Ca values with 23–276 μmol/mol (91.6 μmol/mol average). Still, the average is higher than *N. stella*'s by a factor of at least three, despite the higher ambient pore-water [Mn] in SBB (5–25 μmol/l), suggesting a difference in element fractionation during biomineralization between these two species.

Element fractionation in coprecipitation with calcite is described by partition coefficients (also distribution coefficient or D_{Mn}), expressed by the ratio of foraminiferal-test and pore-water TE/Ca. The SBB's Ca system is spatially uniform and in steady-state (Berelson et al., 2005; Komada et al., 2016), with an average pore-water Ca of 10.2 mmol/kg, as measured within the top two cm of SBB sediments in August 2012 at a site with comparable environmental conditions (590 m water depth, $[O_2]$ = 2 μmol/kg, 6°C; Komada et al., 2016) and in close proximity to the sites in this study. Assuming the same pore-water Ca^{2+} for the time of sampling, we can estimate $Mn/Ca_{pore\text{-}water}$ (0.5–2 mmol/mol) and establish D_{Mn} for *N. stella* (0.02 ± 0.01; Table S4). The estimated D_{Mn} of *N. stella* is substantially lower than of *N. labradorica* (D_{Mn} = 1.24; Koho et al., 2017) and remains at the lower end of previously reported values also compared to other benthic (0.09–0.62 in Barras et al., 2018; ~1 in Glock et al., 2012, Koho et al., 2015; 0.02–1.77 in Koho et al., 2017; 2.6–10 in Munsel et al., 2010) and planktonic foraminifera (0.2–2; Steinhardt et al., 2014).

Previous studies indicated that Mn fractionation in foraminifera might depend on ambient Mn availability, with increasing D_{Mn} towards low $Mn/Ca_{sea\text{-}water}$ (Barras et al., 2018). The same trend is present in our data of *N. stella*, with its D_{Mn} depending on ambient pore-water Mn/Ca ($p < 0.0002$; Welch test) in inverse correlation (based on individual Mn/Ca_{foram}: $r = -0.53$, $p < 0.0001$; based on average Mn/Ca_{foram}: $r = -0.90$, $p = 0.0009$; linear fit; Figure S4). Assuming *N. stella* follows the same exponential trend as observed for *A. tepida* in Barras et al. (2018; see Appendix 4 therein), its D_{Mn} might stabilize around 0.01 at higher pore-water [Mn].

We note that our interpretation of *N. stella*'s D_{Mn} is limited by the facts that *in situ* pore-water [Mn] and Mn/Ca_{foram} may not be precisely coupled (see also discussion Section 5.2), the $Mn_{pore\text{-}water}$ range is restricted (i.e., < 15 μmol/l), and the assumed pore-water [Ca] may not be consistent with actual [Ca] of our study sites. Further studies under controlled conditions and/or time-series measurements of pore-water [Mn] during the growth of chambers are needed to resolve the exact relationship between Mn availability and uptake by *N. stella*. Nevertheless, a species-specific control on Mn partitioning for *N. stella* is evident, which again highlights the need for species-specific proxy calibrations.

6. Conclusions

Through a multidisciplinary approach combining molecular and morphological taxonomic characterization and ion beam- and synchrotron-based techniques we explored the low-oxygen proxy-potential of *Nonionella stella* in a modern field-study in the SBB. Based on both morphological and genetic criteria, we assigned *N. stella* specimens of the SBB to a new phylotype, T6. Due to comparably low incorporation of Mn, we conclude that *N. stella/N.* sp. T6 is not ideal as a Mn/Ca proxy, at least under BWO < 10 μmol/l (i.e., suboxic) and low pore-water dissolved [Mn] (< 25 μmol/l) as encountered in the SBB.

Distribution mapping and *in situ* analysis of Mn/Ca show high inter- and intra-specimen Mn/Ca heterogeneity, that must be explained by both environment-driven and intrinsic variability. This highlights the need for species-specific proxy calibrations and a robust understanding of the average test geochemistry. Uncertainties in the interpretation of foraminiferal Mn/Ca trends may be reduced through multiple measurements per specimen and use of several specimens per sample.

Investigations of paired hydrographic and geochemical parameters of the SBB underline the complexity of sedimentary and biogenic processes in TE cycling and uptake. Our data show that average pore-water Mn is uncorrelated with BWO, and the relationship to foraminiferal Mn/Ca counters theoretical expectations (these would predict that increasing availability of dissolved Mn causes increased uptake). We conclude that under suboxic conditions, the sensitivity of the Mn/Ca low-oxygen proxy appears reduced and its interpretation is not straightforward without considerations of local and regional redox dynamics and oxygenation regimes. Still, the correlation of Mn uptake with bottom-water oxygenation changes suggests potential of the foraminiferal Mn/Ca proxy in general. Additional calibration studies over wide oxygen gradients representative of coastal marine settings are required for the further development of the foraminiferal Mn/Ca proxy and to pave the way for robust paleo-reconstructions of severely oxygen-depleted conditions.

Acknowledgments
We thank the Captain and crew of the R/V '*Robert Gordon Sproul*' for technical assistance during sample collection. We thank Tomas Naera (Department for Geology, Lund University, Sweden) for assisting with the OKA characterization, as well as guidance during mount polishing; Kerstin Lindén for help with SIMS sample preparation; Heejin Jeon for technical guidance during SIMS analysis (both NordSIMS, Naturhistoriska Riksmuseet Stockholm, Sweden); John W. Walley and Mike Spicuzza (Department of Geoscience, University of Wisconsin, USA) for providing the UWC-3 standard. Further thanks go to Thierry Jauffrais (Unité Lagons, Ecosystèmes et Aquaculture Durable en Nouvelle-Calédonie, Ifremer, New-Caledonia) for help picking live *Nonionella*, Sophie Quinchard (LPG-BIAF, University of Angers) for technical help in molecular work and Romain Mallet (SCIAM, University of Angers) for SEM images. We also thank Dirk Müter for helpful discussions regarding image analyzes. Finally, we thank the editor and two anonymous reviewers whose comments helped to improve this manuscript. We acknowledge funding from the Swedish Research Council VR (grant numbers 2017-04190 and 2017-00671), the Crafoord Foundation, and the Royal Physiographic Society in Lund, Sweden. Shiptime provided by US NSF IOS 1557430. We acknowledge SOLEIL for provision of synchrotron radiation facilities and the beamline NANOSCOPIUM (proposal number 20181115). The synchrotron-based experiments were supported by CALIPSOplus under the EU Framework Programme for Research and Innovation HORIZON 2020 (grant agreement 730872). The SIMS analyses were jointly supported by the Swedish Museum of Natural History and Swedish Research Council. This is NordSIMS contribution No. 694. J. M. Bernhard and C. M. Hansel also acknowledge funding from the US National Science Foundation (IOS 1557430).

Data Availability Statement

Open Research: The data generated during this study is archived at the Swedish National Data Service (SND) and available under https://doi.org/10.5878/x6sa-jy16.

References

Aller, R. C., Charnock, H., Edmond, J. M., McCave, I. N., Rice, A. L., & Wilson, T. R. S. (1990). Bioturbation and manganese cycling in hemipelagic sediments. *Philosophical Transactions of the Royal Society of London, Series A, Mathematical and Physical Sciences*, *331*(1616), 51–68. https://doi.org/10.1098/rsta.1990.0056

Altenbach, A. V., Leiter, C., Mayr, C., Struck, U., Hiss, M., & Radic, A. (2012). Carbon and nitrogen isotopic fractionation in foraminifera: Possible signatures from anoxia. In A. V. Altenbach, J. M. Bernhard, & J. Seckbach (Eds.), *Anoxia: Evidence for eukaryote survival and paleontological strategies* (pp. 515–535). Dordrecht: Springer Netherlands. https://doi.org/10.1007/978-94-007-1896-8_27

Anderson, M. J. (2017). Permutational multivariate analysis of variance (PERMANOVA). In N. Balakrishnan, T. Colton, B. Everitt, W. Piegorsch, F. Ruggeri, & J. L. Teugels (Eds.), *Wiley StatsRef: Statistics reference online* (pp. 1–15). https://doi.org/10.1002/9781118445112.stat07841

Asteman, I. P., & Schönfeld, J. (2016). Recent invasion of the foraminifer *Nonionella stella* Cushman & Moyer, 1930 in northern European waters: Evidence from the Skagerrak and its fjords. *Journal of Micropalaeontology*, *35*(1), 20–007. https://doi.org/10.1144/jmpaleo2015-007

Balestra, B., Orland, I. J., Fessenden-Rahn, J., Gorski, G., Franks, R., Rahn, T., & Paytan, A. (2020). Paired analyses of oxygen isotope and elemental ratios within individual shells of benthic foraminifera genus *Uvigerina*. *Chemical Geology*, *533*, 119377. https://doi.org/10.1016/j.chemgeo.2019.119377

Barras, C., Aurélia, M., Pia, N. M., Edouard, M., Jassin, P., & Carole, L. (2018). Experimental calibration of manganese incorporation in foraminiferal calcite. *Geochimica et Cosmochimica Acta*, *237*, 49–64. https://doi.org/10.1016/j.gca.2018.06.009

Berelson, W. M., Prokopenko, M., Sansone, F. J., Graham, A. W., McManus, J., & Bernhard, J. M. (2005). Anaerobic diagenesis of silica and carbon in continental margin sediments: Discrete zones of TCO_2 production. *Geochimica et Cosmochimica Acta*, *69*(19), 4611–4629. https://doi.org/10.1016/j.gca.2005.05.011

Bernhard, J. M. (2018). *CTD (Sea-Bird SBE-911+) data as collected during the cruise SP1811, Collaborative Research: Physiological plasticity and response of benthic foraminifera to oceanic deoxygenation*. Rolling Deck to Repository (R2R). https://doi.org/10.7284/908085

Bernhard, J. M., Blanks, J. K., Hintz, C. J., & Chandler, G. T. (2004). Use of the fluorescent calcite marker calcein to label foraminiferal tests. *Journal of Foraminiferal Research*, *34*(2), 96–101. https://doi.org/10.2113/0340096

Bernhard, J. M., Edgcomb, V. P., Casciotti, K. L., McIlvin, M. R., & Beaudoin, D. J. (2012). Denitrification likely catalyzed by endobionts in an allogromiid foraminifer. *The ISME Journal*, *6*(5), 951–960. https://doi.org/10.1038/ismej.2011.171

Bernhard, J. M., Goldstein, S. T., & Bowser, S. S. (2010). An ectobiont-bearing foraminiferan, *Bolivina pacifica*, that inhabits microxic pore waters: Cell-biological and paleoceanographic insights. *Environmental Microbiology*, *12*(8), 2107–2119. https://doi.org/10.1111/j.1462-2920.2009.02073.x

Bernhard, J. M., Habura, A., & Bowser, S. S. (2006). An endobiont-bearing allogromiid from the Santa Barbara Basin: Implications for the early diversification of foraminifera. *Journal of Geophysical Research: Biogeosciences*, *111*(G3). https://doi.org/10.1029/2005JG000158

Bernhard, J. M., Ostermann, D. R., Williams, D. S., & Blanks, J. K. (2006). Comparison of two methods to identify live benthic foraminifera: A test between Rose Bengal and CellTracker Green with implications for stable isotope paleoreconstructions. *Paleoceanography*, *21*(4), PA4210. https://doi.org/10.1029/2006PA001290

Bernhard, J. M., & Reimers, C. E. (1991). Benthic foraminiferal population fluctuations related to anoxia: Santa Barbara Basin. *Biogeochemistry*, *15*(2), 127–149. https://doi.org/10.1007/BF00003221

Bernhard, J. M., Sen Gupta, B. K., & Borne, P. F. (1997). Benthic foraminiferal proxy to estimate dysoxic bottom-water oxygen concentrations; Santa Barbara Basin, US Pacific continental margin. *Journal of Foraminiferal Research*, *27*(4), 301–310. https://doi.org/10.2113/gsjfr.27.4.301

Bernhard, J. M., Visscher, P. T., & Bowser, S. S. (2003). Submillimeter life positions of bacteria, protists, and metazoans in laminated sediments of the Santa Barbara Basin. *Limnology & Oceanography*, *48*(2), 813–828. https://doi.org/10.4319/lo.2003.48.2.0813

Bird, C., Schweizer, M., Roberts, A., Austin, W. E. N., Knudsen, K. L., Evans, K. M., et al. (2020). The genetic diversity, morphology, biogeography, and taxonomic designations of *Ammonia* (Foraminifera) in the Northeast Atlantic. *Marine Micropaleontology*, *155*, 101726. https://doi.org/10.1016/j.marmicro.2019.02.001

Bograd, S. J., Schwing, F. B., Castro, C. G., & Timothy, D. A. (2002). Bottom water renewal in the Santa Barbara Basin. *Journal of Geophysical Research: Oceans*, *107*(C12), 3216. https://doi.org/10.1029/2001JC001291

Boyle, E. A. (1983). Manganese carbonate overgrowths on foraminifera tests. *Geochimica et Cosmochimica Acta*, *47*(10), 1815–1819. https://doi.org/10.1016/0016-7037(83)90029-7

Boyle, E. A., & Keigwin, L. (1985). Comparison of Atlantic and Pacific paleochemical records for the last 215,000 years: Changes in deep ocean circulation and chemical inventories. *Earth and Planetary Science Letters*, *76*(1–2), 135–150. https://doi.org/10.1016/0012-821X(85)90154-2

Bray, N. A., Keyes, A., & Morawitz, W. M. L. (1999). The California Current System in the Southern California Bight and the Santa Barbara Channel. *Journal of Geophysical Research: Oceans*, *104*(C4), 7695–7714. https://doi.org/10.1029/1998JC900038

Burdige, D. J. (1993). The biogeochemistry of manganese and iron reduction in marine sediments. *Earth-Science Reviews*, *35*(3), 249–284. https://doi.org/10.1016/0012-8252(93)90040-E

Burdige, D. J., & Gieskes, J. (1983). A pore water/solid phase diagenetic model for manganese in marine sediments. *American Journal of Science*, *283*(1), 29–47. https://doi.org/10.2475/ajs.283.1.29

CalCOFI. (2015). *California cooperative oceanic Fisheries Investigations (2015–2019), data reports, station '081.8 046.9'*. Retrieved from https://calcofi.org/ccdata/database.html

Chen, W., & Simonetti, A. (2013). In-situ determination of major and trace elements in calcite and apatite, and U–Pb ages of apatite from the Oka carbonatite complex: Insights into a complex crystallization history. *Chemical Geology*, *353*, 151–172. https://doi.org/10.1016/j.chemgeo.2012.04.022

Corliss, B., & Silva, K. A. (1993). Rapid growth of deep-sea benthic foraminifera. *Geology*, *21*(11), 991–994. https://doi.org/10.1130/0091-7613(1993)021<0991:rgodsb>2.3.co;2

Cushman, J. A. (1947). New species and varieties of foraminifera from off the southeastern coast of the United States. *Contributions from the Cushman Laboratory for Foraminiferal Research*, 23(8), 86–92.

Cushman, J. A., & Moyer, D. A. (1930). Some Recent foraminifera from off San Pedro, California. *Cushman Laboratory for Foraminiferal Research Contributions* (pp. 49–62).

Darling, K. F., Schweizer, M., Knudsen, K. L., Evans, K. M., Bird, C., Roberts, A., et al. (2016). The genetic diversity, phylogeography and morphology of Elphidiidae (Foraminifera) in the Northeast Atlantic. *Marine Micropaleontology*, *129*, 1–23. https://doi.org/10.1016/j.marmicro.2016.09.001

Davis, C. V., Fehrenbacher, J. S., Benitez-Nelson, C., & Thunell, R. C. (2020). Trace element heterogeneity across individual planktic foraminifera from the modern Cariaco Basin. *Journal of Foraminiferal Research*, *50*(2), 204–218. https://doi.org/10.2113/gsjfr.50.2.204

de Nooijer, L. J., Spero, H. J., Erez, J., Bijma, J., & Reichart, G. J. (2014). Biomineralization in perforate foraminifera. *Earth-Science Reviews*, *135*, 48–58. https://doi.org/10.1016/j.earscirev.2014.03.013

de Nooijer, L. J., Toyofuku, T., & Kitazato, H. (2009). Foraminifera promote calcification by elevating their intracellular pH. *Proceedings of the National Academy of Sciences*, *106*(36), 15374–15378. https://doi.org/10.1073/pnas.0904306106

de Villiers, S. (2005). Foraminiferal shell-weight evidence for sedimentary calcite dissolution above the lysocline. *Deep Sea Research Part I: Oceanographic Research Papers*, *52*(5), 671–680. https://doi.org/10.1016/j.dsr.2004.11.014

Delaney, M. L., Bé, A. W. H., & Boyle, E. A. (1985). Li, Sr, Mg, and Na in foraminiferal calcite shells from laboratory culture, sediment traps, and sediment cores. *Geochimica et Cosmochimica Acta*, *49*(6), 1327–1341. https://doi.org/10.1016/0016-7037(85)90284-4

Deldicq, N., Alve, E., Schweizer, M., Polovodova Asteman, I., Hess, S., Darling, K., & Bouchet, V. M. P. (2019). History of the introduction of a species resembling benthic foraminifera *Nonionella stella* in the Oslofjord (Norway): Morphological, molecular and paleo-ecological evidences. *Aquatic Invasions*, *14*(2), 182–205. https://doi.org/10.3391/ai.2019.14.2.03

Diz, P., Barras, C., Geslin, E., Reichart, G.-J., Metzger, E., Jorissen, F., & Bijma, J. (2012). Incorporation of Mg and Sr and oxygen and carbon stable isotope fractionation in cultured *Ammonia tepida*. *Marine Micropaleontology*, *92*(93), 16–28. https://doi.org/10.1016/j.marmicro.2012.04.006

Elderfield, H., Bertram, C. J., & Erez, J. (1996). Biomineralization model for the incorporation of trace elements into foraminiferal calcium carbonate. *Earth and Planetary Science Letters*, *142*(3–4), 409–423. https://doi.org/10.1016/0012-821X(96)00105-7

Elderfield, H., Vautravers, M., & Cooper, M. (2002). The relationship between shell size and Mg/Ca, Sr/Ca, $\delta^{18}O$, and $\delta^{13}C$ of species of planktonic foraminifera. *Geochemistry, Geophysics, Geosystems*, *3*(8), 1–13. https://doi.org/10.1029/2001GC000194

Emmer, E., & Thunell, R. C. (2000). Nitrogen isotope variations in Santa Barbara Basin sediments: Implications for denitrification in the eastern tropical North Pacific during the last 50,000 years. *Paleoceanography*, *15*(4), 377–387. https://doi.org/10.1029/1999PA000417

Epstein, S., Buchsbaum, R., Lowenstam, H., & Urey, H. C. (1951). Carbonate-water isotopic temperature scale. *GSA Bulletin*, *62*(4), 417–426. https://doi.org/10.1130/0016-7606(1951)62[417:cits]2.0.co;2

Erez, J. (2003). The source of ions for biomineralization in foraminifera and their implications for paleoceanographic proxies. *Reviews in Mineralogy and Geochemistry*, *54*, 115–149. https://doi.org/10.2113/0540115

Filipsson, H. L., Bernhard, J. M., Lincoln, S. A., & McCorkle, D. C. (2010). A culture-based calibration of benthic foraminiferal paleotemperature proxies: Delta O-18 and Mg/Ca results. *Biogeosciences*, *7*, 1335–1347. https://doi.org/10.5194/bg-7-1335-2010

Glock, N., Eisenhauer, A., Liebetrau, V., Wiedenbeck, M., Hensen, C., & Nehrke, G. (2012). EMP and SIMS studies on Mn/Ca and Fe/Ca systematics in benthic foraminifera from the Peruvian OMZ: A contribution to the identification of potential redox proxies and the impact of cleaning protocols. *Biogeosciences*, *9*(1), 341–359. https://doi.org/10.5194/bg-9-341-2012

Glock, N., Liebetrau, V., Vogts, A., & Eisenhauer, A. (2019). Organic heterogeneities in foraminiferal calcite traced through the distribution of N, S, and I measured with NanoSIMS: A new challenge for element-ratio-based paleoproxies? *Frontiers of Earth Science*, *7*, 175. https://doi.org/10.3389/feart.2019.00175

Goldberg, T., Archer, C., Vance, D., Thamdrup, B., McAnena, A., & Poulton, S. W. (2012). Controls on Mo isotope fractionations in a Mn-rich anoxic marine sediment, Gullmar Fjord, Sweden. *Chemical Geology*, *296–297*, 73–82. https://doi.org/10.1016/j.chemgeo.2011.12.020

Gouy, M., Guindon, S., & Gascuel, O. (2010). SeaView version 4: A multiplatform graphical user interface for sequence alignment and phylogenetic tree building. *Molecular Biology and Evolution*, *27*(2), 221–224. https://doi.org/10.1093/molbev/msp259

Groeneveld, J., & Filipsson, H. L. (2013). Mg/Ca and Mn/Ca ratios in benthic foraminifera: The potential to reconstruct past variations in temperature and hypoxia in shelf regions. *Biogeosciences*, *10*(7), 5125–5138. https://doi.org/10.5194/bg-10-5125-2013

Groeneveld, J., Filipsson, H. L., Austin, W. E., Darling, K., McCarthy, D., Krupinski, N. B. Q., et al. (2018). Assessing proxy signatures of temperature, salinity, and hypoxia in the Baltic Sea through foraminifera-based geochemistry and faunal assemblages. *Journal of Micropalaeontology*, *37*, 403–429. https://doi.org/10.5194/jm-37-403-2018

Guo, X., Xu, B., Burnett, W. C., Yu, Z., Yang, S., Huang, X., et al. (2019). A potential proxy for seasonal hypoxia: LA-ICP-MS Mn/Ca ratios in benthic foraminifera from the Yangtze River Estuary. *Geochimica et Cosmochimica Acta*, *245*, 290–303. https://doi.org/10.1016/j.gca.2018.11.007

Halpern, B. S., Walbridge, S., Selkoe, K. A., Kappel, C. V., Micheli, F., D'Agrosa, C., et al. (2008). A global map of human impact on marine ecosystems. *Science*, *319*(5865), 948–952. https://doi.org/10.1126/science.1149345

Hammer, O., Harper, D. A. T., & Ryan, P. D. (2001). PAST: Paleontological statistics software package for education and data analysis. *Palaeontologia Electronica*, *4*(1), 1–9.

Harms, S., & Winant, C. D. (1998). Characteristic patterns of the circulation in the Santa Barbara Channel. *Journal of Geophysical Research*, *103*(C2), 3041–3065. https://doi.org/10.1029/97JC02393

Hayward, B. W., Coze, F. L., Vandepitte, L., & Vanhoorne, B. (2020). Foraminifera in the world register of marine species (Worms) taxonomic database. *Journal of Foraminiferal Research*, *50*(3), 291–300. https://doi.org/10.2113/gsjfr.50.3.291

Hayward, B. W., Holzmann, M., Grenfell, H. R., Pawlowski, J., & Triggs, C. M. (2004). Morphological distinction of molecular types in *Ammonia*: Towards a taxonomic revision of the world's most commonly misidentified foraminifera. *Marine Micropaleontology*, *50*(3–4), 237–271. https://doi.org/10.1016/S0377-8398(03)00074-4

Hintz, C. J., Shaw, T. J., Chandler, G. T., Bernhard, J. M., McCorkle, D. C., & Blanks, J. K. (2006). Trace/minor element: Calcium ratios in cultured benthic foraminifera. Part I: Inter-species and inter-individual variability. *Geochimica et Cosmochimica Acta*, *70*(8), 1952–1963. https://doi.org/10.1016/j.gca.2005.12.018

Holzmann, M., & Pawlowski, J. (2017). An updated classification of rotaliid foraminifera based on ribosomal DNA phylogeny. *Marine Micropaleontology*, *132*, 18–34. https://doi.org/10.1016/j.marmicro.2017.04.002

Ivanochko, T. S., & Pedersen, T. F. (2004). Determining the influences of Late Quaternary ventilation and productivity variations on Santa Barbara Basin sedimentary oxygenation: A multi-proxy approach. *Quaternary Science Reviews*, *23*(3–4), 467–480. https://doi.org/10.1016/j.quascirev.2003.06.006

Jenkins, R. (1995). *Quantitative X-ray Spectrometry*. Boca Raton, FL: CRC Press.

Jochum, K. P., Nohl, U., Herwig, K., Lammel, E., Stoll, B., & Hofmann, A. W. (2005). GeoReM: A New Geochemical Database for Reference Materials and Isotopic Standards. *Geostandards and Geoanalytical Research*, *29*, 333–338. https://doi.org/10.1111/j.1751-908x.2005.tb00904.x

Jorissen, F. J., Fontanier, C., & Thomas, E. (2007). Chapter Seven: Paleoceanographical proxies based on deep-sea benthic foraminiferal assemblage characteristics. In C. Hillaire–Marcel, & A. de Vernal (Eds.), *Proxies in late cenozoic Paleoceanography: Pt. 2: Biological tracers and biomarker* (pp. 263–325). Amsterdam: Elsevier. https://doi.org/10.1016/S1572-5480(07)01012-3

Jorissen, F. J., Wittling, I., Peypouquet, J. P., Rabouille, C., & Relexans, J. C. (1998). Live benthic foraminiferal faunas off Cape Blanc, NW-Africa: Community structure and microhabitats. *Deep Sea Research Part I: Oceanographic Research Papers*, *45*(12), 2157–2188. https://doi.org/10.1016/S0967-0637(98)00056-9

Kawahata, H. (2019). Climatic reconstruction at the Sannai-Maruyama site between Bond events 4 and 3: Implication for the collapse of the society at 4.2kaevent. *Progress in Earth and Planetary Science*, *6*(1), 63. https://doi.org/10.1186/s40645-019-0308-8

Keeling, R. F., & Garcia, H. E. (2002). The change in oceanic O_2 inventory associated with recent global warming. *Proceedings of the National Academy of Sciences*, *99*(12), 7848–7853. https://doi.org/10.1073/pnas.122154899

Keul, N., Langer, G., de Nooijer, L. J., & Bijma, J. (2013). Effect of ocean acidification on the benthic foraminifera *Ammonia* sp. is caused by a decrease in carbonate ion concentration. *Biogeosciences*, *10*(10), 6185–6198. https://doi.org/10.5194/bg-10-6185-2013

Kienast, S. S., Calvert, S. E., & Pedersen, T. F. (2002). Nitrogen isotope and productivity variations along the northeast Pacific margin over the last 120 kyr: Surface and subsurface paleoceanography. *Paleoceanography*, *17*(4), 1055. https://doi.org/10.1029/2001PA000650

Klinkhammer, G. P., Mix, A. C., & Haley, B. A. (2009). Increased dissolved terrestrial input to the coastal ocean during the last deglaciation. *Geochemistry, Geophysics, Geosystems*, *10*(3), Q03009. https://doi.org/10.1029/2008gc002219

Koho, K. A., de Nooijer, L. J., Fontanier, C., Toyofuku, T., Oguri, K., Kitazato, H., & Reichart, G.-J. (2017). Benthic foraminiferal Mn/Ca ratios reflect microhabitat preferences. *Biogeosciences*, *14*(12), 3067–3082. https://doi.org/10.5194/bg-14-3067-2017

Koho, K. A., de Nooijer, L. J., & Reichart, G.-J. (2015). Combining benthic foraminiferal ecology and shell Mn/Ca to deconvolve past bottom water oxygenation and paleoproductivity. *Geochimica et Cosmochimica Acta*, *165*, 294–306. https://doi.org/10.1016/j.gca.2015.06.003

Komada, T., Burdige, D. J., Li, H.-L., Magen, C., Chanton, J. P., & Cada, A. K. (2016). Organic matter cycling across the sulfate-methane transition zone of the Santa Barbara Basin, California Borderland. *Geochimica et Cosmochimica Acta*, *176*, 259–278. https://doi.org/10.1016/j.gca.2015.12.022

Kozdon, R., Ushikubo, T., Kita, N. T., Spicuzza, M., & Valley, J. W. (2009). Intratest oxygen isotope variability in the planktonic foraminifer *N. pachyderma*: Real vs. apparent vital effects by ion microprobe. *Chemical Geology*, *258*(3), 327–337. https://doi.org/10.1016/j.chemgeo.2008.10.032

Kuwabara, J. S., van Geen, A., McCorkle, D. C., & Bernhard, J. M. (1999). Dissolved sulfide distributions in the water column and sediment pore waters of the Santa Barbara Basin. *Geochimica et Cosmochimica Acta*, *63*(15), 2199–2209. https://doi.org/10.1016/S0016-7037(99)00084-8

Law, G. T., Shimmield, T. M., Shimmield, G. B., Cowie, G. L., Breuer, E. R., & Harvey, S. M. (2009). Manganese, iron, and sulphur cycling on the Pakistan margin. *Deep Sea Research Part II: Topical Studies in Oceanography*, *56*(6–7), 305–323. https://doi.org/10.1016/j.dsr2.2008.06.011

Lea, D. W., Mashiotta, T. A., & Spero, H. J. (1999). Controls on magnesium and strontium uptake in planktonic foraminifera determined by live culturing. *Geochimica et Cosmochimica Acta*, *63*(16), 2369–2379. https://doi.org/10.1016/S0016-7037(99)00197-0

Lenz, C., Jilbert, T., Conley, D. J., & Slomp, C. P. (2015). Hypoxia-driven variations in iron and manganese shuttling in the Baltic Sea over the past 8 kyr. *Geochemistry, Geophysics, Geosystems*, *16*(10), 3754–3766. https://doi.org/10.1002/2015GC005960

Levin, L. A., & Breitburg, D. L. (2015). Linking coasts and seas to address ocean deoxygenation. *Nature Climate Change*, *5*(5), 401–403. https://doi.org/10.1038/nclimate2595

Livsey, C. M., Kozdon, R., Bauch, D., Brummer, G.-J. A., Jonkers, L., Orland, I., et al. (2020). High-resolution Mg/Ca and $\delta^{18}O$ patterns in modern *Neogloboquadrina pachyderma* from the Fram Strait and Irminger Sea. *Paleoceanography and Paleoclimatology*, *35*, e2020PA003969. https://doi.org/10.1029/2020PA003969

Luther, G. W., Sundby, B., Lewis, B. L., Brendel, P. J., & Silverberg, N. (1997). Interactions of manganese with the nitrogen cycle: Alternative pathways to dinitrogen. *Geochimica et Cosmochimica Acta*, *61*(19), 4043–4052. https://doi.org/10.1016/S0016-7037(97)00239-1

Lynn, R. J., & Simpson, J. J. (1987). The California Current System: The seasonal variability of its physical characteristics. *Journal of Geophysical Research: Oceans*, *92*(C12), 12947–12966. https://doi.org/10.1029/JC092iC12p12947

Mackensen, A., Schumacher, S., Radke, J., & Schmidt, D. N. (2000). Microhabitat preferences and stable carbon isotopes of endobenthic foraminifera: Clue to quantitative reconstruction of oceanic new production? *Marine Micropaleontology*, *40*(3), 233–258. https://doi.org/10.1016/S0377-8398(00)00040-2

Madison, A. S., Tebo, B. M., & Luther, G. W. (2011). Simultaneous determination of soluble manganese(III), manganese(II) and total manganese in natural (pore)waters. *Talanta*, *84*(2), 374–381. https://doi.org/10.1016/j.talanta.2011.01.025

Mashiotta, T. A., Lea, D. W., & Spero, H. J. (1999). Glacial–interglacial changes in subantarctic sea surface temperature and δ^{18}O-water using foraminiferal Mg. *Earth and Planetary Science Letters*, *170*(4), 417–432. https://doi.org/10.1016/S0012-821X(99)00116-8

McCorkle, D. C., Keigwin, L. D., Corliss, B. H., & Emerson, S. R. (1990). The influence of microhabitats on the carbon isotopic composition of deep-sea benthic foraminifera. *Paleoceanography*, *5*(2), 161–185. https://doi.org/10.1029/PA005i002p00161

McDonald, J. H. (2014). *One way anova. Handbook of biological statistics*. Baltimore, MD: Sparky House Publishing.

McKay, C. L., Groeneveld, J., Filipsson, H. L., Gallego-Torres, D., Whitehouse, M. J., Toyofuku, T., & Romero, O. E. (2015). A comparison of benthic foraminiferal Mn/Ca and sedimentary Mn/Al as proxies of relative bottom-water oxygenation in the low-latitude NE Atlantic upwelling system. *Biogeosciences*, *12*(18), 5415–5428. https://doi.org/10.5194/bg-12-5415-2015

Medjoubi, K., Leclercq, N., Langlois, F., Buteau, A., Lé, S., Poirier, S., et al. (2013). Development of fast parallel multi-technique scanning X-ray imaging at Synchrotron Soleil. *Journal of Physics: Conference Series*, *463*, 012031. https://doi.org/10.1088/1742-6596/463/1/012031

Munsel, D., Kramar, U., Dissard, D., Nehrke, G., Berner, Z., Bijma, J., et al. (2010). Heavy metal incorporation in foraminiferal calcite: Results from multi-element enrichment culture experiments with *Ammonia tepida*. *Biogeosciences*, *7*(8), 2339–2350. https://doi.org/10.5194/bg-7-2339-2010

Murray, J. W. (2014). *Ecology and palaeoecology of benthic foraminifera*. London: Routledge.

Ní Fhlaithearta, S., Fontanier, C., Jorissen, F., Mouret, A., Dueñas-Bohórquez, A., Anschutz, P., et al. (2018). Manganese incorporation in living (stained) benthic foraminiferal shells: A bathymetric and in-sediment study in the Gulf of Lions (NW Mediterranean). *Biogeosciences*, *15*(20), 6315–6328. https://doi.org/10.5194/bg-15-6315-2018

Ní Fhlaithearta, S., Reichart, G. J., Jorissen, F. J., Fontanier, C., Rohling, E. J., Thomson, J., & de Lange, G. J. (2010). Reconstructing the seafloor environment during sapropel formation using benthic foraminiferal trace metals, stable isotopes, and sediment composition. *Paleoceanography*, *25*(4), PA4225. https://doi.org/10.1029/2009pa001869

Nørvang, A. (1945). *The zoology of Iceland: Foraminifera*. Copenhagen & Reykjavik: Ejnar Munksgaard.

Nürnberg, D., Buma, J., & Hemleben, C. (1996). Assessing the reliability of magnesium in foraminiferal calcite as a proxy for water mass temperatures. *Geochimica et Cosmochimica Acta*, *60*(5), 803–814. https://doi.org/10.1016/0016-7037(95)00446-7

Ohkouchi, N., Kawahata, H., Murayama, M., Okada, M., Nakamura, T., & Taira, A. (1994). Was deep water formed in the North Pacific during the Late Quaternary? Cadmium evidence from the Northwest Pacific. *Earth and Planetary Science Letters*, *124*(1), 185–194. https://doi.org/10.1016/0012-821X(94)00082-4

Oldham, V. E., Mucci, A., Tebo, B. M., & Luther, G. W. (2017). Soluble Mn(III)–L complexes are abundant in oxygenated waters and stabilized by humic ligands. *Geochimica et Cosmochimica Acta*, *199*, 238–246. https://doi.org/10.1016/j.gca.2016.11.043

Oldham, V. E., Owings, S. M., Jones, M. R., Tebo, B. M., & Luther, G. W. (2015). Evidence for the presence of strong Mn(III)-binding ligands in the water column of the Chesapeake Bay. *Marine Chemistry*, *171*, 58–66. https://doi.org/10.1016/j.marchem.2015.02.008

Orland, I. J., Burstyn, Y., Bar-Matthews, M., Kozdon, R., Ayalon, A., Matthews, A., & Valley, J. W. (2014). Seasonal climate signals (1990–2008) in a modern Soreq Cave stalagmite as revealed by high-resolution geochemical analysis. *Chemical Geology*, *363*, 322–333. https://doi.org/10.1016/j.chemgeo.2013.11.011

Paton, C., Hellstrom, J., Paul, B., Woodhead, J., & Hergt, J. (2011). Iolite: Freeware for the visualisation and processing of mass spectrometric data. *Journal of Analytical Atomic Spectrometry*, *26*, 2508–2518. https://doi.org/10.1039/C1JA10172B

Pawlowski, J. (2000). Introduction to the molecular systematics of foraminifera. *Micropaleontology*, *46*, 1–12.

Pawlowski, J., & Holzmann, M. (2014). A plea for DNA barcoding of foraminifera. *Journal of Foraminiferal Research*, *44*(1), 62–67. https://doi.org/10.2113/gsjfr.44.1.62

Pearson, P. N. (2012). Oxygen isotopes in foraminifera: Overview and historical review. *Paleontological Society Papers*, *18*, 1–38. https://doi.org/10.1017/S1089332600002539

Petersen, J., Barras, C., Bézos, A., La, C., de Nooijer, L. J., Meysman, F. J. R., et al. (2018). Mn/Ca intra- and inter-test variability in the benthic foraminifer *Ammonia tepida*. *Biogeosciences*, *15*(1), 331–348. https://doi.org/10.5194/bg-15-331-2018

Petersen, J., Barras, C., Bézos, A., La, C., Slomp, C. P., Meysman, F. J. R., et al. (2019). Mn/Ca ratios of Ammonia tepida as a proxy for seasonal coastal hypoxia. *Chemical Geology*, *518*, 55–66. https://doi.org/10.1016/j.chemgeo.2019.04.002

Raitzsch, M., Dueñas-Bohórquez, A., Reichart, G.-J., de Nooijer, L. J., & Bickert, T. (2010). Incorporation of Mg and Sr in calcite of cultured benthic foraminifera: Impact of calcium concentration and associated calcite saturation state. *Biogeosciences*, *7*(3), 869–881. https://doi.org/10.5194/bg-7-869-2010

Reichart, G.-J., Jorissen, F., Anschutz, P., & Mason, P. R. D. (2003). Single foraminiferal test chemistry records the marine environment. *Geology*, *31*(4), 355–358. https://doi.org/10.1130/0091-7613(2003)031<0355:sftcrt>2.0.co;2

Reimers, C. E., Lange, C. B., Tabak, M., & Bernhard, J. M. (1990). Seasonal spillover and varve formation in the Santa Barbara Basin, California. *Limnology & Oceanography*, *35*(7), 1577–1585. https://doi.org/10.4319/lo.1990.35.7.1577

Reimers, C. E., Ruttenberg, K. C., Canfield, D. E., Christiansen, M. B., & Martin, J. B. (1996). Porewater pH and authigenic phases formed in the uppermost sediments of the Santa Barbara Basin. *Geochimica et Cosmochimica Acta*, *60*(21), 4037–4057. https://doi.org/10.1016/S0016-7037(96)00231-1

Remmelzwaal, S. R. C., Sadekov, A. Y., Parkinson, I. J., Schmidt, D. N., Titelboim, D., Abramovich, S., et al. (2019). Post-depositional overprinting of chromium in foraminifera. *Earth and Planetary Science Letters*, *515*, 100–111. https://doi.org/10.1016/j.epsl.2019.03.001

Rhein, M., Rintoul, S. R., Aoki, S., Campos, E., Chambers, D., Feely, R. A., et al. (2013). Observations: Ocean. In T. F. Stocker, D. Qin, G.-K. Plattner, M. Tignor, S. K. Allen, J. Boschung, et al. (Eds.), *Climate change 2013: The physical science basis. Contribution of working group I to the fifth assessment report of the intergovernmental panel on climate change*. Cambridge and New York, NY: Cambridge University Press.

Richirt, J., Schweizer, M., Bouchet, V. M. P., Mouret, A., Quinchard, S., & Jorissen, F. J. (2019). Morphological distinction of three *Ammonia* phylotypes occurring along European coasts. *Journal of Foraminiferal Research*, *49*(1), 76–93. https://doi.org/10.2113/gsjfr.49.1.76

Roberts, A., Austin, W., Evans, K., Bird, C., Schweizer, M., & Darling, K. (2016). A new integrated approach to taxonomy: The fusion of molecular and morphological systematics with type material in benthic foraminifera. *PLoS One*, *11*(7), e0158754. https://doi.org/10.1371/journal.pone.0158754

Rueden, C. T., Schindelin, J., Hiner, M. C., DeZonia, B. E., Walter, A. E., Arena, E. T., & Eliceiri, K. W. (2017). ImageJ2: ImageJ for the next generation of scientific image data. *BMC Bioinformatics*, *18*(1), 529. https://doi.org/10.1186/s12859-017-1934-z

Sadekov, A., Eggins, S. M., Deckker, P. D., & Kroon, D. (2008). Uncertainties in seawater thermometry deriving from intratest and intertest Mg/Ca variability in *Globigerinoides ruber*. *Paleoceanography*, *23*(1), PA1215. https://doi.org/10.1029/2007PA001452

Schindelin, J., Arganda-Carreras, I., Frise, E., Kaynig, V., Longair, M., Pietzsch, T., et al. (2012). Fiji: An open-source platform for biological-image analysis. *Nature Methods*, *9*(7), 676–682. https://doi.org/10.1038/nmeth.2019

Schweizer, M., Pawlowski, J., Duijnstee, I. A. P., Kouwenhoven, T. J., & van der Zwaan, G. J. (2005). Molecular phylogeny of the foraminiferal genus *Uvigerina* based on ribosomal DNA sequences. *Marine Micropaleontology*, *57*(3), 51–67. https://doi.org/10.1016/j.marmicro.2005.07.001

Solé, V. A., Papillon, E., Cotte, M., Walter, P., & Susini, J. (2007). A multiplatform code for the analysis of energy-dispersive X-ray fluorescence spectra. *Spectrochimica Acta Part B: Atomic Spectroscopy*, *62*(1), 63–68. https://doi.org/10.1016/j.sab.2006.12.002

Somogyi, A., Medjoubi, K., Baranton, G., Le Roux, V., Ribbens, M., Polack, F., et al. (2015). Optical design and multi-length-scale scanning spectro-microscopy possibilities at the Nanoscopium beamline of Synchrotron Soleil. *Journal of Synchrotron Radiation*, *22*(4), 1118–1129. https://doi.org/10.1107/S1600577515009364

Steinhardt, J., Cléroux, C., Ullgren, J., de Nooijer, L., Durgadoo, J. V., Brummer, G.-J., & Reichart, G.-J. (2014). Anti-cyclonic eddy imprint on calcite geochemistry of several planktonic foraminiferal species in the Mozambique Channel. *Marine Micropaleontology*, *113*, 20–33. https://doi.org/10.1016/j.marmicro.2014.09.001

Stookey, L. L. (1970). Ferrozine: A new spectrophotometric reagent for iron. *Analytical Chemistry*, *42*(7), 779–781. https://doi.org/10.1021/ac60289a016

Sulu-Gambari, F., Roepert, A., Jilbert, T., Hagens, M., Meysman, F. J. R., & Slomp, C. P. (2017). Molybdenum dynamics in sediments of a seasonally-hypoxic coastal marine basin. *Chemical Geology*, *466*, 627–640. https://doi.org/10.1016/j.chemgeo.2017.07.015

Tachikawa, K., & Elderfield, H. (2002). Microhabitat effects on Cd/Ca and $\delta^{13}C$ of benthic foraminifera. *Earth and Planetary Science Letters*, *202*(3), 607–624. https://doi.org/10.1016/S0012-821X(02)00796-3

Thamdrup, B. (2000). Bacterial manganese and iron reduction in aquatic sediments. In B. Schink (Ed.), *Advances in microbial ecology* (pp. 41–84). Boston, MA: Springer US. https://doi.org/10.1007/978-1-4615-4187-5_2

Tribovillard, N., Algeo, T. J., Lyons, T., & Riboulleau, A. (2006). Trace metals as paleoredox and paleoproductivity proxies: An update. *Chemical Geology*, *232*(1–2), 12–32. https://doi.org/10.1016/j.chemgeo.2006.02.012

Trouwborst, R. E., Clement, B. G., Tebo, B. M., Glazer, B. T., & Luther, G. W. (2006). Soluble Mn(III) in suboxic zones. *Science*, *313*(5795), 1955–1957. https://doi.org/10.1126/science.1132876

van der Weijden, C. H., Reichart, G. J., & Visser, H. J. (1999). Enhanced preservation of organic matter in sediments deposited within the oxygen minimum zone in the northeastern Arabian Sea. *Deep Sea Research Part I: Oceanographic Research Papers*, *46*(5), 807–830. https://doi.org/10.1016/S0967-0637(98)00093-4

van Dijk, I., de Nooijer, L. J., Barras, C., & Reichart, G.-J. (2020). Mn incorporation in large benthic Foraminifera: Differences between species and the impact of pCO_2. *Frontiers of Earth Science*, *8*, 567701. https://doi.org/10.3389/feart.2020.567701

van Dijk, I., Mouret, A., Cotte, M., Le Houedec, S., Oron, S., Reichart, G.-J., et al. (2019). Chemical heterogeneity of Mg, Mn, Na, S, and Sr in benthic foraminiferal calcite. *Frontiers of Earth Science*, *7*, 281. https://doi.org/10.3389/feart.2019.00281

van Geen, A., Zheng, Y., Bernhard, J. M., Cannariato, K. G., Carriquiry, J., Dean, W. E., et al. (2003). On the preservation of laminated sediments along the western margin of North America. *Paleoceanography*, *18*(4), 1098. https://doi.org/10.1029/2003PA000911

Vandenabeele, J., de Beer, D., Germonpré, R., Van de Sande, R., & Verstraete, W. (1995). Influence of nitrate on manganese removing microbial consortia from sand filters. *Water Research*, *29*(2), 579–587. https://doi.org/10.1016/0043-1354(94)00173-5

Woodhead, J. D., Hellstrom, J., Hergt, J. M., Greig, A., & Maas, R. (2007). Isotopic and elemental imaging of geological materials by laser ablation Inductively Coupled Plasma mass spectrometry. *Journal of Geostandards and Geoanalytical Research*, *31*(4), 331–343. https://doi.org/10.1111/j.1751-908X.2007.00104.x

Zeebe, R. E., Bijma, J., Hönisch, B., Sanyal, A., Spero, H. J., & Wolf-Gladrow, D. A. (2008). Vital effects and beyond: A modelling perspective on developing palaeoceanographical proxy relationships in foraminifera. *Geological Society, London, Special Publications*, *303*(1), 45–58. https://doi-org.ludwig.lub.lu.se/10.1144/SP303.4

Zheng, Y., Anderson, R. F., van Geen, A., & Kuwabara, J. (2000). Authigenic molybdenum formation in marine sediments: A link to pore water sulfide in the Santa Barbara Basin. *Geochimica et Cosmochimica Acta*, *64*(24), 4165–4178. https://doi.org/10.1016/S0016-7037(00)00495-6